

Wave breaking and formation of dispersive shock waves in a defocusing nonlinear optical materialM. Isoard,¹ A. M. Kamchatnov,^{2,3} and N. Pavloff¹¹*LPTMS, UMR 8626, CNRS, Univ. Paris–Sud, Université Paris–Saclay, 91405 Orsay, France*²*Institute of Spectroscopy, Russian Academy of Sciences, Troitsk, Moscow 108840, Russia*³*Moscow Institute of Physics and Technology, Institutsky Lane 9, Dolgoprudny, Moscow Region 141701, Russia*

(Received 19 February 2019; published 14 May 2019)

We describe theoretically the quasi-one-dimensional transverse spreading of a light beam propagating in a nonlinear optical material in the presence of a uniform background light intensity. For short propagation distances the pulse can be described within a nondispersive (geometric optics) approximation by means of Riemann's approach. For larger distances, wave breaking occurs, leading to the formation of dispersive shocks at both edges of the beam. We describe this phenomenon within Whitham modulation theory, which yields excellent agreement with numerical simulations. Our analytic approach makes it possible to extract the leading asymptotic behavior of the parameters of the shock, setting up the basis for a theory of nondissipative weak shocks.

DOI: [10.1103/PhysRevA.99.053819](https://doi.org/10.1103/PhysRevA.99.053819)**I. INTRODUCTION**

It has long been known that light propagating in a nonlinear medium is amenable to a hydrodynamic treatment (see, e.g., Refs. [1–3]). In the case of a defocusing nonlinearity, this rich analogy has not only triggered experimental research, but also made it possible to get an intuitive understanding of observations of, e.g., the formation of rings in the far field beyond a nonlinear slab [4,5], dark solitons [6–8], vortices [9–11], wave breaking [12,13], dispersive shock waves [14–19], spontaneously self-accelerated Airy beams [20], an optical event horizon [21], ergo regions [22], stimulated Hawking radiation [23], soniclike dispersion relations [24,25], and superfluid motion [26]. Very similar phenomena have also been observed in the neighboring fields of cavity polaritons and Bose-Einstein condensation of atomic vapors. They all result from the interplay between nonlinearity and dispersion, whose effects become prominent near a gradient catastrophe region.

In this work we present a theoretical treatment of a model configuration which has been realized experimentally in a one-dimensional situation in Refs. [15,18]: the nonlinear spreading of a region of increased light intensity in the presence of a uniform constant background. In the absence of background and for a smooth initial intensity pattern, the spreading is mainly driven by the nonlinear defocusing and can be treated analytically in some simple cases [1]. The situation is more interesting in the presence of a constant background: The pulse splits in two parts, each eventually experiencing nonlinear wave breaking, leading to the formation of a dispersive shock wave (DSW) which cannot be described within the framework of perturbation theory, even if the region of increased intensity corresponds to a weak perturbation of the flat pedestal. This scenario indeed fits with the hydrodynamic approach of nonlinear light propagation and is nicely confirmed by the experimental observations of Refs. [15,18]. Although the numerical treatment of the problem is relatively simple [27–29], a theoretical approach to both the initial splitting of the pulse and the subsequent shock

formation requires a careful analysis. The goal of this article is to present such an analysis. A most significant outcome of our detailed treatment is a simple asymptotic description of some important shock parameters. This provides a nondissipative counterpart of the usual weak viscous shock theory (see, e.g., Ref. [30]) and paves the way for a quantitative experimental test of our predictions.

The paper is organized as follows. In Sec. II we present the model and the setup we study. After a brief discussion of the shortcomings of the linearized approach, the spreading and splitting stage of evolution is accounted for in Sec. III within a dispersionless approximation which holds when the pulse region initially presents no large intensity gradient. It is well known that in such a situation the light flow can be described by hydrodynamiclike equations which can be cast into a diagonal form for two new position and time-dependent variables: the so-called Riemann invariants. The difficulty here lies in the fact that the splitting involves simultaneous variations of both of them: One does not have an initial simple wave within which one of the Riemann invariants remains constant, as occurs, for instance, in a similar unidirectional propagation case modeled by the Korteweg–de Vries equation (see, e.g., Ref. [31]). We treat the problem in Secs. III A and III B using an extension of the Riemann method due to Ludford [32] (also used in Ref. [33]) and compare the results with numerical simulations in Sec. III C. During the spreading of the pulse, nonlinear effects induce wave steepening, which results in a gradient catastrophe and wave breaking. After the wave breaking time, dispersive effects can no longer be omitted and a shock is formed; in this case we resort to Whitham modulation theory [30] to describe the time evolution of the pulse. Such a treatment was initiated long ago by Gurevich and Pitaevskii [34], and since that time it has developed into a powerful method with numerous applications (see, e.g., the review article in [35]). Here there is an additional complexity which lies, as for the initial nondispersive stage of evolution, in the fact that two of the (now four) Riemann invariants which describe the modulated nonlinear oscillations vary in

the shock region. Such a wave has been termed quasisimple in Ref. [36], and a thorough treatment within Whitham theory has been achieved in the Korteweg–de Vries case in Refs. [37–40]. In Sec. IV we generalize this approach to the nonlinear Schrödinger equation (NLS), which describes light propagation in the nonlinear Kerr medium (see also Ref. [41]). An interesting outcome of our theoretical treatment is the asymptotic determination of experimentally relevant parameters of the dispersive shock (Sec. V). In Sec. VI we present the full Whitham treatment of the after-shock evolution and compare the theoretical results with numerical simulations. We present in Sec. VII a panorama of the different regimes we have identified and discuss how our approach can be used to get a simple estimate of the contrast of the fringes of the DSW. This should be helpful in determining the best experimental configuration for studying the wave breaking phenomenon and the subsequent dispersive shock. Our conclusions and a summary of our results are presented in Sec. VIII.

II. MODEL AND LINEAR APPROXIMATION

In the paraxial approximation, the stationary propagation of the complex amplitude $A(\vec{r})$ of the electric field of a monochromatic beam is described by the equation (see, e.g., Ref. [42])

$$i\partial_z A = -\frac{1}{2n_0 k_0} \nabla_{\perp}^2 A - k_0 \delta n A. \quad (1)$$

In this equation, n_0 is the linear refractive index, $k_0 = 2\pi/\lambda_0$ is the carrier wave vector, z is the coordinate along the beam, ∇_{\perp}^2 is the transverse Laplacian, and δn is a nonlinear contribution to the index. In a nonabsorbing defocusing Kerr nonlinear medium we can write $\delta n = -n_2 |A|^2$, with $n_2 > 0$.

We define dimensionless units by choosing a reference intensity I_{ref} and introducing the nonlinear length $z_{\text{NL}} = (k_0 n_2 I_{\text{ref}})^{-1}$ and the transverse healing length $\xi_{\perp} = (z_{\text{NL}}/n_0 k_0)^{1/2}$. We consider a geometry where the transverse profile is translationally invariant and depends on a single Cartesian coordinate. We thus write $\nabla_{\perp}^2 = \xi_{\perp}^{-2} \partial_x^2$, where x is the dimensionless transverse coordinate and we define an effective time $t = z/z_{\text{NL}}$. The quantity $\psi(x, t) = A/\sqrt{I_{\text{ref}}}$ is then a solution of the dimensionless NLS equation

$$i\psi_t = -\frac{1}{2}\psi_{xx} + |\psi|^2\psi. \quad (2)$$

In the following we consider a system with a uniform background light intensity, on top of which an initial pulse is added at the entrance of the nonlinear cell. The initial $\psi(x, t = 0)$ is real (i.e., no transverse velocity or, in an optical context, no focusing of the light beam at the input plane), with a dimensionless intensity $\rho(x, t) = |\psi|^2$ which departs from the constant background value (which we denote by ρ_0) only in the region near the origin where it forms a bump. To be specific, we consider the typical case where

$$\rho(x, 0) = \begin{cases} \rho_0 + \rho_1(1 - x^2/x_0^2) & \text{if } |x| < x_0 \\ \rho_0 & \text{if } |x| \geq x_0. \end{cases} \quad (3)$$

The maximal density of the initial profile is defined as $\rho_m = \rho_0 + \rho_1$. It would be natural to choose the reference light intensity I_{ref} to be equal to the background one; in this case

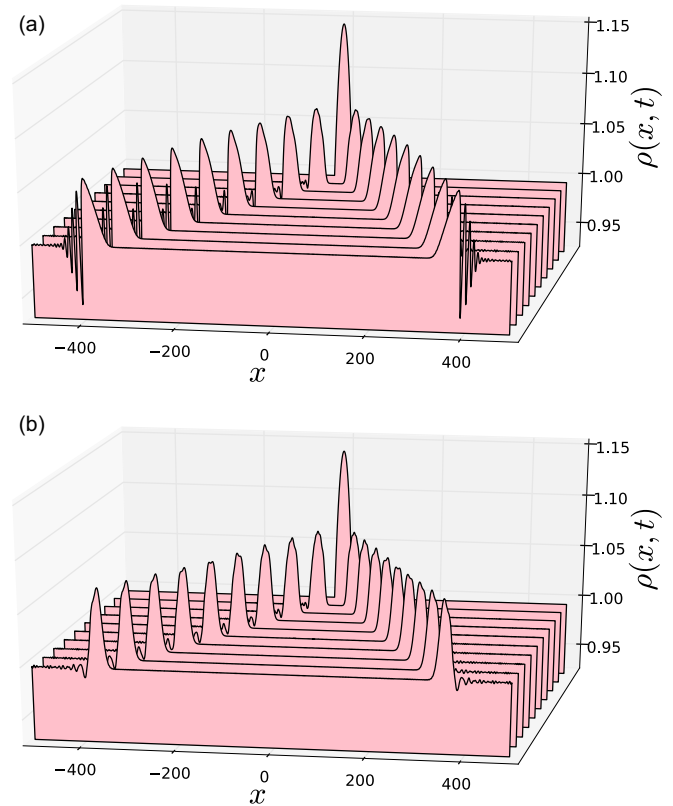


FIG. 1. Density profiles $\rho(x, t)$ for an initial condition $u(x, 0) = 0$ and $\rho(x, 0)$ given by (3) with $\rho_0 = 1$, $\rho_1 = 0.15$, and $x_0 = 20$. Results are shown for (a) the numerical solution of Eq. (2) and (b) the linearized version (4). The profiles are plotted from time $t = 0$ to $t = 360$ with a time step equal to 40.

we would have $\rho_0 = 1$. However, we prefer to be more general and to allow for values of ρ_0 different from unity.

We stress here the paramount importance of nonlinear effects for large time, i.e., for large propagation distance in the nonlinear medium. Even for a bump which weakly departs from the background density, a perturbative approach fails after the wave breaking time. This is illustrated in Fig. 1, which compares numerical simulations of the full Eq. (2) with its linearized version. The linearized treatment is obtained by writing $\psi(x, t) = \exp(-i\rho_0 t)[\sqrt{\rho_0} + \delta\psi(x, t)]$ and assuming that $|\delta\psi|^2 \ll \rho_0$, which yields the evolution equation

$$i\partial_t \delta\psi = -\frac{1}{2}\partial_x^2 \delta\psi + \rho_0(\delta\psi + \delta\psi^*) \quad (4)$$

and then $\rho(x, t) \simeq \rho_0 + \sqrt{\rho_0}(\delta\psi + \delta\psi^*)$. In the case illustrated in Fig. 1, the initial profile has, at its maximum, a weak 15% density increase with respect to the background. The initial splitting of the bump is correctly described by the linearized approach, but after the wave breaking time the linearized evolution goes on predicting a roughly global displacement of the two humps at constant velocity (with additional small dispersive corrections) and clearly fails to reproduce both the formation of DSWs and the stretching of the dispersionless part of the profile (which reaches a quasitriangular shape).

III. DISPERSIONLESS STAGE OF EVOLUTION

In view of the shortcomings of the linearized approximation illustrated in Fig. 1, we include nonlinear effects at all stages of the dynamical study of the model. By means of the Madelung substitution

$$\psi(x, t) = \sqrt{\rho(x, t)} \exp\left(i \int^x u(x', t) dx'\right), \quad (5)$$

the NLS equation (2) can be cast into a hydrodynamiclike form for the density $\rho(x, t)$ and the flow velocity $u(x, t)$:

$$\begin{aligned} \rho_t + (\rho u)_x &= 0, \\ u_t + uu_x + \rho_x + \left(\frac{\rho_x^2}{8\rho^2} - \frac{\rho_{xx}}{4\rho}\right)_x &= 0. \end{aligned} \quad (6)$$

These equations are to be solved with the initial conditions (3) and $u(x, 0) = 0$.

The last term on the left-hand side of the second of Eqs. (6) accounts for the dispersive character of the fluid of light. In the first stage of spreading of the bump, if the density gradients of the initial density are weak, i.e., if $x_0 \gg \max\{\rho_0^{-1/2}, \rho_1^{-1/2}\}$, the effects of dispersion can be neglected and the system (6) then simplifies to

$$\rho_t + (\rho u)_x = 0, \quad u_t + uu_x + \rho_x = 0. \quad (7)$$

These equations can be written in a more symmetric form by introducing the Riemann invariants

$$\lambda^\pm(x, t) = \frac{u(x, t)}{2} \pm \sqrt{\rho(x, t)}, \quad (8)$$

which evolve according to the system [equivalent to (7)]

$$\partial_t \lambda^\pm + v_\pm(\lambda^-, \lambda^+) \partial_x \lambda^\pm = 0, \quad (9)$$

with

$$v_\pm(\lambda^-, \lambda^+) = \frac{1}{2}(3\lambda^\pm + \lambda^\mp) = u \pm \sqrt{\rho}. \quad (10)$$

The Riemann velocities (10) have a simple physical interpretation for a smooth velocity and density distribution: v_+ (v_-) corresponds to a signal which propagates downstream (upstream) at the local velocity of sound $c = \sqrt{\rho}$ and which is dragged by the background flow u .

The system (9) can be linearized by means of the hodograph transform (see, e.g., Ref. [43]), which consists in considering x and t as functions of λ^+ and λ^- . We readily obtain

$$\partial_\pm x - v_\mp \partial_\pm t = 0, \quad (11)$$

where $\partial_\pm \equiv \partial/\partial\lambda^\pm$. We introduce two auxiliary (yet unknown) functions $W_\pm(\lambda^+, \lambda^-)$ such that

$$x - v_\pm(\lambda^-, \lambda^+)t = W_\pm(\lambda^-, \lambda^+). \quad (12)$$

Inserting the above expressions in (11) shows that the W^\pm are solutions of Tsarev equations [44]

$$\frac{\partial_- W_+}{W_+ - W_-} = \frac{\partial_- v_+}{v_+ - v_-}, \quad \frac{\partial_+ W_-}{W_+ - W_-} = \frac{\partial_+ v_-}{v_+ - v_-}. \quad (13)$$

From Eqs. (10) and (13) we can verify that $\partial_- W_+ = \partial_+ W_-$, which shows that W_+ and W_- can be sought in the form

$$W_\pm = \partial_\pm \chi, \quad (14)$$

where $\chi(\lambda^-, \lambda^+)$ plays the role of a potential. Substituting expressions (14) in one of the Tsarev equations shows that χ is a solution of the Euler-Poisson equation

$$\frac{\partial^2 \chi}{\partial \lambda^+ \partial \lambda^-} - \frac{1}{2(\lambda^+ - \lambda^-)} \left(\frac{\partial \chi}{\partial \lambda^+} - \frac{\partial \chi}{\partial \lambda^-} \right) = 0, \quad (15)$$

which can be written under the standard form

$$\frac{\partial^2 \chi}{\partial \lambda^+ \partial \lambda^-} + a(\lambda^-, \lambda^+) \frac{\partial \chi}{\partial \lambda^+} + b(\lambda^-, \lambda^+) \frac{\partial \chi}{\partial \lambda^-} = 0, \quad (16)$$

with

$$a(\lambda^-, \lambda^+) = -b(\lambda^-, \lambda^+) = -\frac{1}{2(\lambda^+ - \lambda^-)}. \quad (17)$$

A. Solution of the Euler-Poisson equation

We can use Riemann's method to solve Eq. (16) in the (λ^+, λ^-) plane, which we refer to below as the characteristic plane. We follow here the procedure given in Refs. [32,33], which applies to nonmonotonic initial distributions, such as the one corresponding to Eq. (3).

We first schematically depict in Fig. 2 the initial spatial distributions $\lambda^\pm(x, 0)$ of the Riemann invariants [Fig. 2(a)] and their later typical time evolution [Figs. 2(b) and 2(c)]. We introduce notation for several special initial values of the Riemann invariants: $\lambda^\pm(-x_0, 0) = \lambda^\pm(x_0, 0) = \pm\sqrt{\rho_0} = \pm c_0$ and $\lambda^\pm(0, 0) = \pm\sqrt{\rho_m} = \pm c_m$. We also define as part A (B) the branch of the distribution of the λ^\pm which is at the right (left) of the extremum. All the notation is summarized in Fig. 2(a).

At a given time, the x axis can be considered as divided into five domains, each requiring a specific treatment. Each region is characterized by the behavior of the Riemann invariant and is identified in Figs. 2(b) and 2(c). The domains in which both Riemann invariants depend on position are labeled by arabic numbers and the ones in which only one Riemann invariant depends on x are labeled by roman numbers. For instance, in region III, λ^+ is a decreasing function of x while $\lambda^- = -c_0$ is a constant; in region 3, λ^+ is decreasing while λ^- is increasing; in region 2 both are increasing; etc.

The values of the Riemann invariants at time corresponding to Fig. 2(b) are represented in the characteristic plane in Fig. 3(a). In this plot the straight solid lines correspond to the simple-wave regions (I and III) while the curvy lines corresponds to regions where both Riemann invariants depend on position: domains 1, 2, and 3. In each of these three domains the solution χ of the Euler-Poisson equation has a different expression. In order to describe these three branches, following Ludford [32], we introduce several sheets in the characteristic plane by unfolding the domain $[c_0, c_m] \times [-c_m, -c_0]$ into a four times larger region as illustrated in Fig. 3(b). The potential $\chi(\lambda^-, \lambda^+)$ can now take a different form in each of the regions labeled 1, 2, and 3 in Fig. 3(b) and still be considered as single valued.

We consider a flow where initially $u(x, 0) = 0$, which implies that $\lambda^+(x, 0) = -\lambda^-(x, 0)$. This condition defines the

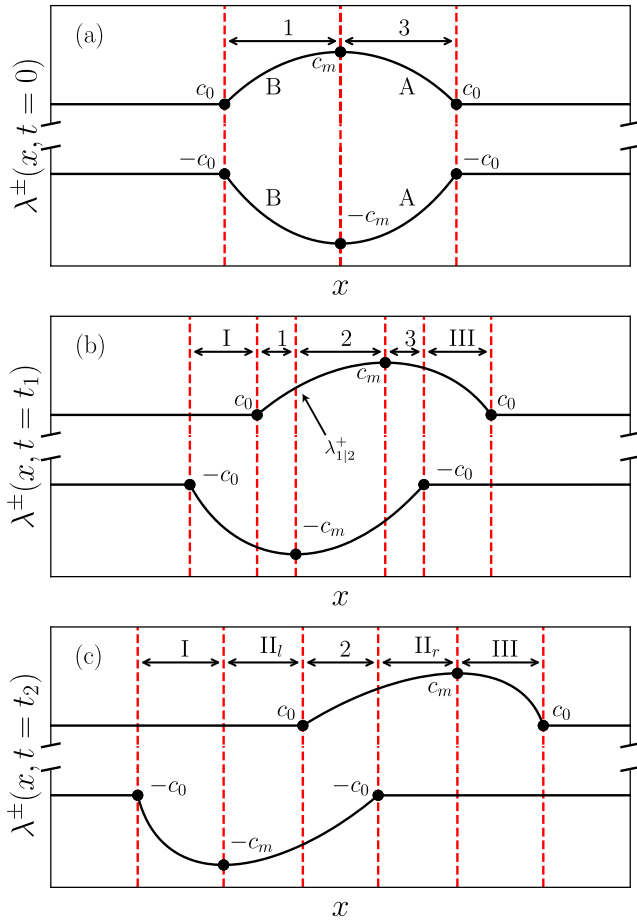


FIG. 2. Sketch of the distributions $\lambda^\pm(x, t)$ at several times. In each panel the top solid curve represent λ^+ (always larger than c_0) and the bottom one λ^- (always lower than $-c_0$), both plotted as functions of x . (a) Initial distribution, in which part B corresponds to region 1 and part A to region 3 (see the text). Two subsequent relevant stages of evolution are represented in (b) and (c). They correspond to times $t_1 < t_{\text{sw}}(c_m) < t_2$, where $t_{\text{sw}}(c_m)$ is defined in Sec. III B (see also Fig. 4). For $t > 0$, λ^+ (λ^-) moves to the right (to the left) and part B of λ^+ starts to overlap with part A of λ^- . This behavior initially leads to the configuration represented in (b), where a new region (labeled region 2) has appeared. For later convenience, we spot in this panel the value $\lambda_{1|2}^+(t_1)$ of the Riemann invariant λ^+ at the boundary between regions 1 and 2 (see the discussion in Sec. III C). For longer time [in (c)], region 2 remains while regions 1 and 3 vanish and new simple-wave regions II_l and II_r appear. At even larger times (not represented), region 2 also vanishes and only simple-wave regions remain: The initial pulse has split into two simple-wave pulses propagating in opposite directions.

curve of initial conditions of our problem in the characteristic plane. It is represented by a red solid curve labeled C^0 in Fig. 3. We remark here that the whole region above C^0 [shaded in Fig. 3(b)] is unreachable for the initial distribution we consider: For instance, the upper shaded triangle in region 1 would correspond to a configuration in which $\lambda_{\text{region1}}^+(x, t) > |\lambda_{\text{region1}}^-(x, t)|$, which does not occur in our case [see Fig. 2(b)].

Before establishing that the expression for χ is the three relevant regions of Fig. 3, it is convenient to define the inverse

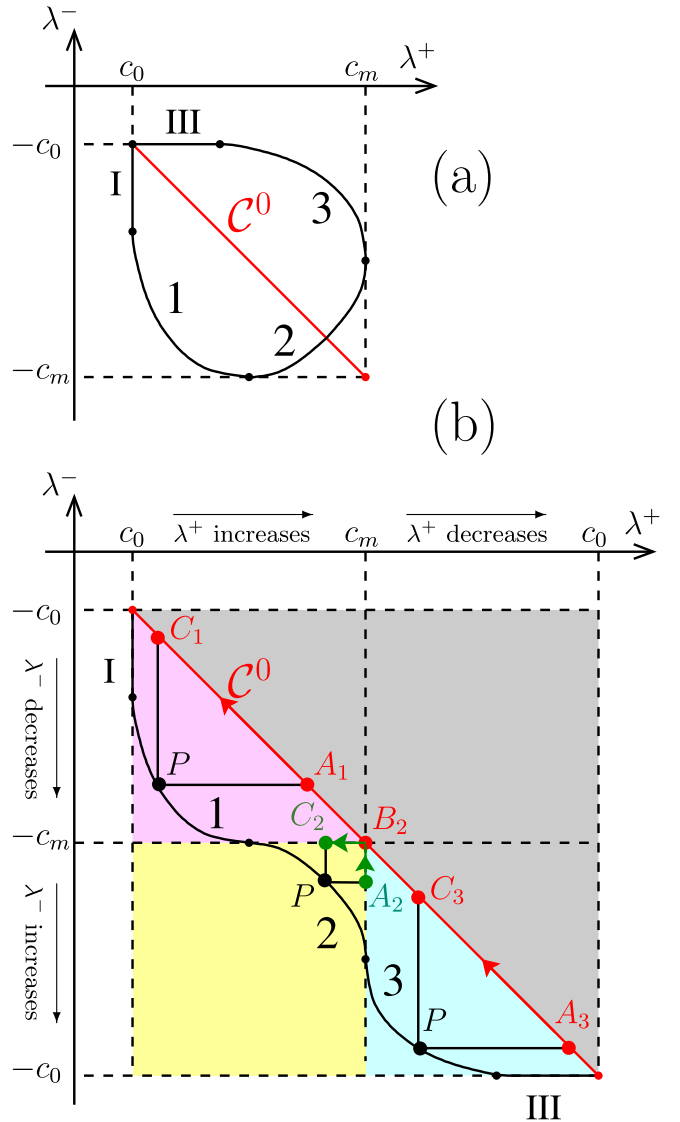


FIG. 3. (a) Behavior of the Riemann invariants in the characteristic plane at a given time t . (b) Same curve on the four-sheeted unfolded surface. The red curve C^0 corresponds to the initial condition $[\lambda^-(x, 0) = -\lambda^+(x, 0)]$. At later time, the relation between $\lambda^+(x, t)$ and $\lambda^-(x, t)$ is given by the black solid curve, which is denoted by C^t in the text. A generic point P of C^t has coordinates (λ^+, λ^-) and points C_1, A_1, B_2, C_3 , and A_3 lie on the initial curve C^0 . Points A_2 and C_2 lie on a boundary between two regions. The arrows indicate the direction of integration in Eqs. (21) and (28). In our problem, the whole gray shaded domain above C^0 is unreachable.

functions of the initial λ profiles in both parts A and B of Fig. 2(a). The symmetry of the initial conditions makes it possible to use the same functions for $\lambda^+ \in [c_0, c_m]$ and $\lambda^- \in [-c_m, -c_0]$:

$$x = \begin{cases} w^A(\lambda^\pm) = x_0 \sqrt{1 - \frac{(\lambda^\pm)^2 - \rho_0}{\rho_m - \rho_0}} & \text{if } x > 0 \\ w^B(\lambda^\pm) = -x_0 \sqrt{1 - \frac{(\lambda^\pm)^2 - \rho_0}{\rho_m - \rho_0}} & \text{if } x < 0. \end{cases} \quad (18)$$

For $t = 0$, using Eqs. (12) and (14), the boundary conditions read

$$\frac{\partial \chi}{\partial \lambda^\pm} \Big|_{\lambda^\pm(x,t=0)} = x = w^{A(B)}(\lambda^\pm), \quad (19)$$

where the superscript B holds in region 1 (when $x < 0$) and A holds in region 3 ($x > 0$). Formula (19) requires some explanation: Its left-hand side is a function of two variables λ^+ and λ^- which is evaluated for $\lambda^- = -\lambda^+$; its right-hand side is expressed by the same function in terms of λ^+ or λ^- since the functions w^A and w^B depend only on the square of their argument. The boundary conditions (19) correspond to a potential χ which takes the form along C^0 ,

$$\begin{aligned} \chi^{(n)}(\lambda^- = -\lambda^+, \lambda^+) \\ = \int_{c_0}^{\lambda^+} w^{A(B)}(r)dr + \int_{-\lambda^+}^{\lambda^-} w^{A(B)}(r)dr, \end{aligned} \quad (20)$$

where $n = 1$ or 3 and, on the right-hand side, the superscript A (B) holds when $n = 3$ ($n = 1$). For the specific initial condition we consider [$u(x, 0) \equiv 0$ and $\rho(x, 0)$ an even function of x], w^A and w^B are even functions and thus our choice of integration constants yields $\chi = 0$ along C^0 .

Let us now consider a point P , lying in either region 1 or 3 (the case of region 2 is considered later), with coordinates (λ^+, λ^-) in the characteristic plane. We introduce points A_1, A_3, C_1 , and C_3 which are located on the curve C^0 , with geometrical definitions obvious from Fig. 3(b). Note the different subscripts for C and A : Subscript 1 (3) is to be used if P is in region 1 (3). We can obtain the value of χ at the point P from Riemann's method (see, e.g., Ref. [45]); the general solution reads

$$\begin{aligned} \chi^{(n)}(P) = \frac{1}{2}\chi(C_n)R(C_n) + \frac{1}{2}\chi(A_n)R(A_n) \\ - \int_{A_n}^{C_n} V dr + U ds, \end{aligned} \quad (21)$$

with

$$\begin{aligned} U(s, r) = \frac{1}{2} \left(R \frac{\partial \chi}{\partial s} - \chi \frac{\partial R}{\partial s} \right) + aR\chi, \\ V(s, r) = \frac{1}{2} \left(\chi \frac{\partial R}{\partial r} - R \frac{\partial \chi}{\partial r} \right) - bR\chi, \end{aligned} \quad (22)$$

where

$$R(s, r) = \frac{2}{\pi} \sqrt{\frac{r-s}{\lambda^+ - \lambda^-}} \mathbf{K}[m(s, r)], \quad (23)$$

with \mathbf{K} the complete elliptic integral of the first kind and

$$m(s, r) = \frac{(\lambda^+ - r)(\lambda^- - s)}{(r - s)(\lambda^+ - \lambda^-)} \quad (24)$$

the associated parameter (we follow here the convention of Ref. [46]). In our case, the symmetries of the initial profile lead to many simplifications in formulas (21) and (22). Along the curve C^0 we have $\chi = 0$. This implies that $\chi^{(n)}(A_n) = \chi^{(n)}(C_n) = 0$, and along the integration path going from A_n to C_n we have

$$U = \frac{1}{2} w^{A(B)}(r)R(s = -r, r) = -V, \quad (25)$$

where the superscript A (B) holds when P is in region 3 (region 1). Explicit evaluation of expression (21) then yields

$$\chi^{(n)}(P) = \frac{2\sqrt{2}}{\pi\sqrt{\lambda^+ - \lambda^-}} \int_{-\lambda^-}^{\lambda^+} \sqrt{r} \mathbf{K}[m(r)] w^{A(B)}(r) dr, \quad (26)$$

where

$$m(r) \equiv m(-r, r) = \frac{(\lambda^+ - r)(\lambda^- + r)}{2r(\lambda^+ - \lambda^-)}. \quad (27)$$

To calculate $\chi(P)$ in region 2 we define three points: A_2, B_2 , and C_2 [see Fig. 3(b)]. Point B_2 is on the curve C^0 , at the junction between regions 1, 2, and 3. Point A_2 lies on the characteristic curve $\lambda^+ = c_m$, on the boundary between regions 2 and 3, whereas point C_2 lies on the characteristic $\lambda^- = -c_m$, on the boundary between regions 1 and 2. Then, from Eqs. (21)–(24), we can easily find that in region 2,

$$\begin{aligned} \chi^{(2)}(P) = \chi(B_2)R(B_2) + \int_{B_2}^{C_2} \left(\frac{\partial \chi}{\partial r} + b\chi \right) R_1(r) dr \\ - \int_{A_2}^{B_2} \left(\frac{\partial \chi}{\partial s} + a\chi \right) R_2(s) ds, \end{aligned} \quad (28)$$

where

$$\begin{aligned} R_1(r) \equiv \frac{2}{\pi} \sqrt{\frac{r+c_m}{\lambda^+ - \lambda^-}} \mathbf{K}[m_1(r)], \\ m_1(r) = \frac{(r-\lambda^+)(c_m+\lambda^-)}{(r-\lambda^-)(\lambda^+ + c_m)} \end{aligned} \quad (29)$$

and

$$\begin{aligned} R_2(s) = \frac{2}{\pi} \sqrt{\frac{c_m-s}{\lambda^+ - \lambda^-}} \mathbf{K}[m_2(s)], \\ m_2(s) = \frac{(c_m-\lambda^+)(\lambda^- - s)}{(c_m-\lambda^-)(\lambda^+ - s)}. \end{aligned} \quad (30)$$

Note that in formula (28) we have $\chi(B_2) = 0$ and the value of χ along the integration lines B_2C_2 and A_2B_2 is known from the previous result (26). After some computation we eventually get the expression for $\chi(P)$ in region 2,

$$\begin{aligned} \chi^{(2)}(P) = \frac{2\sqrt{2}}{\pi\sqrt{\lambda^+ - \lambda^-}} \left[\int_{c_m}^{\lambda^+} \sqrt{r} \mathbf{K}[m_0(r; \lambda^+)] w^B(r) dr \right. \\ \left. + \int_{-\lambda^-}^{c_m} \sqrt{r} \mathbf{K}[m_0(r; -\lambda^-)] w^A(r) dr \right] \\ + \frac{4\sqrt{2}}{\pi^2\sqrt{\lambda^+ - \lambda^-}} \left[\int_{c_m}^{\lambda^+} \sqrt{r} w^B(r) f_1(r) dr \right. \\ \left. + \int_{-\lambda^-}^{c_m} \sqrt{r} w^A(r) f_2(r) dr \right], \end{aligned} \quad (31)$$

where we have introduced the notation

$$\begin{aligned} f_1(r) = \int_{\lambda^+}^r \mathbf{K}[m_0(r; u)] \frac{\partial \mathbf{K}[m_1(u)]}{\partial u} du, \\ f_2(r) = \int_{-\lambda^-}^r \mathbf{K}[m_0(r; u)] \frac{\partial \mathbf{K}[m_2(-u)]}{\partial u} du, \end{aligned} \quad (32)$$

with

$$m_0(r; u) = \frac{(r-u)(c_m-r)}{2r(u+c_m)}. \quad (33)$$

In many instances we can actually simplify the expressions (26) and (31): for reasonable values of c_m (chosen to be of same order as c_0 in our simulations) the elliptic integral $K(m)$ turns out to be approximately equal to $\pi/2$ for all points P in the three regions. In this case, the exact expressions (26) and (31) can be replaced by a simple approximation $\chi(P) \simeq \chi_{\text{app}}(P)$ which reads, when P is in region $n = 1$ or 3,

$$\chi_{\text{app}}^{(n)}(\lambda_-, \lambda_+) = \frac{\sqrt{2}}{\sqrt{\lambda^+ - \lambda^-}} \int_{-\lambda^-}^{\lambda^+} \sqrt{r} w^{A(B)}(r) dr, \quad (34)$$

where the superscript A (B) holds when $n = 3$ ($n = 1$). When P is in region 2 we get

$$\begin{aligned} \chi_{\text{app}}^{(2)}(\lambda_-, \lambda_+) &= \frac{\sqrt{2}}{\sqrt{\lambda^+ - \lambda^-}} \int_{c_m}^{\lambda^+} \sqrt{r} w^B(r) dr \\ &+ \frac{\sqrt{2}}{\sqrt{\lambda^+ - \lambda^-}} \int_{-\lambda^-}^{c_m} \sqrt{r} w^A(r) dr. \end{aligned} \quad (35)$$

This approximation greatly simplifies the numerical determination of the integrals involved in the solution of the problem. We have checked that it is very accurate in all the configurations we study in the present work. The reason for its validity is easy to understand in regions 1 and 3: The argument of the elliptic integral K in Eq. (26) is zero at the two boundaries of the integration domain ($r = -\lambda^-$ and $r = \lambda^+$) and reaches a maximum when $r = \sqrt{-\lambda^- \lambda^+}$, taking the value

$$0 \leq m_{\text{max}} = \frac{1}{2} \left(1 - \frac{2\sqrt{-\lambda^- \lambda^+}}{\lambda^+ - \lambda^-} \right) \leq \frac{1}{2}. \quad (36)$$

As time varies, the largest value of m_{max} is reached at the point where region 3 disappears, when $\lambda^+ = c_m$ and $\lambda^- = -c_0$. For $c_m/c_0 \sim 1$ this value is typically much lower than the upper bound $\frac{1}{2}$ of Eq. (36). For instance, in the numerical simulations below, we take $\rho_0 = 0.5$ and $\rho_m = 2$ and we get accordingly $c_0 = \sqrt{0.5}$ and $c_m = \sqrt{2}$ and the corresponding largest value of m_{max} is $\simeq 2.9 \times 10^{-2}$.

B. Simple-wave regions

Once χ has been computed in the domains 1, 2, and 3 where two Riemann invariants depend on position, it remains to determine the values of λ^+ and λ^- in the simple-wave regions. Let us focus on, for instance, region III, in which $\lambda^- = -c_0$ and λ^+ depends on x and t . The behavior of the characteristics in the (x, t) plane is sketched in Fig. 4. We see in this figure that the characteristic of a given value of λ^+ enters the simple-wave region III at a given time, which we denote by $t_{\text{SW}}(\lambda^+)$, and a given position $x_{\text{SW}}(\lambda^+)$. Beyond this point the characteristic becomes a straight line and the general solution of Eq. (9) for λ^+ is known to be of the form

$$x - v_+(-c_0, \lambda^+)t = h(\lambda^+), \quad (37)$$

where the unknown function h is determined by boundary conditions. From Eq. (12) we see that just at the boundary between regions 3 and III we have

$$x_{\text{SW}}(\lambda^+) - v_+(-c_0, \lambda^+)t_{\text{SW}}(\lambda^+) = W_+^{(3)}(-c_0, \lambda^+), \quad (38)$$

where $W_+^{(3)} = \partial_+ \chi^{(3)}$. This shows that in Eq. (37) the unknown function $h(\lambda^+)$ is equal to $W_+^{(3)}(-c_0, \lambda^+)$. The

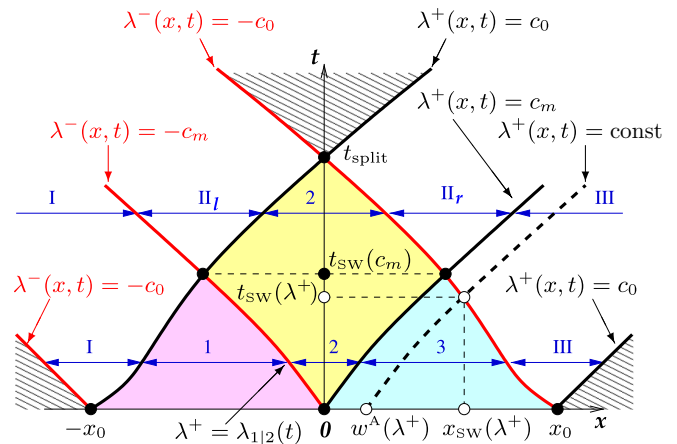


FIG. 4. Sketch of the characteristics in the (x, t) plane. The black (red) solid lines are specific characteristics for λ^+ (λ^-) stemming from the edges of the hump and from its maximum. The thick dashed line is a generic characteristic of λ^+ . In the hatched regions both Riemann invariants are constant [$\lambda^\pm(x, t) = \pm c_0$] and the profile is flat. In the colored regions both Riemann invariants depend on position (the color code is the same as in Fig. 3: region 1 is pink, region 2 is yellow, and region 3 is cyan). In the white regions only one Riemann invariant depends on position: We have a simple wave. The notation is explained in the text.

equation of the characteristic in region III thus reads

$$x - v_+(-c_0, \lambda^+)t = W_+^{(3)}(-c_0, \lambda^+). \quad (39)$$

Similar reasoning shows that in region I we have

$$x - v_- (\lambda^-, c_0)t = W_-^{(1)}(\lambda^-, c_0). \quad (40)$$

For time larger than $t_{\text{SW}}(c_m)$, regions 1 and 3 disappear and two new simple-wave regions appear, which we denote by II_l and II_r [see Fig. 4 and also Fig. 2(c)]. The same reasoning as above shows that in these regions the characteristics are determined by

$$x - v_+(-c_0, \lambda^+)t = W_+^{(2)}(-c_0, \lambda^+) \quad \text{in } \text{II}_r \quad (41)$$

and

$$x - v_- (\lambda^-, c_0)t = W_-^{(2)}(\lambda^-, c_0) \quad \text{in } \text{II}_l. \quad (42)$$

C. Solution of the dispersionless problem and comparison with numerical simulations

The problem is now solved: Having determined χ in regions 1, 2, and 3 (see Sec. III A), we obtain W_\pm in these regions from Eqs. (14).

(i) It is then particularly easy to find the values of λ^+ and λ^- in the simple-wave regions. For instance, in region III, we have $\lambda_- = -c_0$, and for given x and t , λ^+ is obtained from Eq. (39). The same procedure is to be employed in the simple-wave regions I, II_r , and II_l , where the relevant equations are then Eqs. (40), (41), and (42), respectively.

(ii) To determine the values of λ^+ and λ^- as functions of x and t in regions 1, 2, and 3 we follow a different procedure which is detailed below, but which essentially consists in the following: For a given time t and a given region n ($n = 1, 2,$

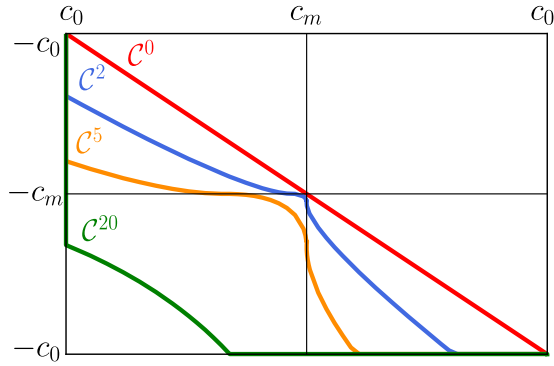


FIG. 5. Theoretical curves C^t representing λ^- as a function of λ^+ at a given time in the characteristic plane. The curves are plotted for $t = 0$ (C^0 , in red), $t = 2$ (blue), $t = 5$ (orange), and $t = 20 > t_{\text{SW}}(c_m)$ (green). The corresponding initial distribution $\lambda^\pm(x, 0)$ is schematically represented in Fig. 2(a). We take here $c_0 = 1/\sqrt{2}$ and $c_m = \sqrt{2}$.

or 3) we pick one of the possible values of λ^+ . From Eqs. (12) λ^- is then solution of

$$\frac{W_+^{(n)}(\lambda^-, \lambda^+) - W_-^{(n)}(\lambda^-, \lambda^+)}{v_+(\lambda^-, \lambda^+) - v_-(\lambda^-, \lambda^+)} + t = 0 \quad (43)$$

and x is determined by either one of Eqs. (12). So, for given t and λ^+ in region n , we have determined the values of λ^- and x . In practice, this makes it possible to associate a couple (λ^-, λ^+) in region n to each (x, t) .

The procedure for determining the profile in regions 1, 2, and 3 which has just been explained has to be implemented with care, because the relevant regions to be considered and their boundaries change with time; for instance, regions 1 and 3 disappear when $t > t_{\text{SW}}(c_m)$. It would be tedious to list here all the possible cases so instead we explain the specifics of the procedure by means of an example: the determination of λ^+ and λ^- in region 1 when $t < t_{\text{SW}}(c_m)$.

We start by determining the value of λ^+ along the characteristic $\lambda^- = -c_m$ at time t (see Fig. 4). This value of λ^+ defines the boundary between regions 1 and 2 and we accordingly denote it by $\lambda_{1|2}^+(t)$; it is represented in Fig. 2(b). From Eqs. (12) it is a solution of

$$\frac{W_+^{(1)}(-c_m, \lambda_{1|2}^+) - W_-^{(1)}(-c_m, \lambda_{1|2}^+)}{v_+(-c_m, \lambda_{1|2}^+) - v_-(-c_m, \lambda_{1|2}^+)} + t = 0. \quad (44)$$

We then know that, in region 1, at time t , λ^+ takes all possible values between c_0 and $\lambda_{1|2}^+(t)$. Having determined the precise range of variation of λ^+ we can now, for each possible λ^+ , determine λ^- from Eq. (43) (with $n = 1$) and follow the above-explained procedure.

(iii) The approach described in the present section makes it possible to determine the curve C^t representing, at time t , the profile in the unfolded characteristic plane. A sketch of C^t was given in Fig. 3(b); it is now precisely represented in Fig. 5 for several values of t , along with the initial curve C^0 .

Once λ^+ and λ^- have been determined as functions of x and t , the density and velocity profiles are obtained through Eqs. (8). We obtain an excellent description of the initial dispersionless stage of evolution of the pulse, as demonstrated

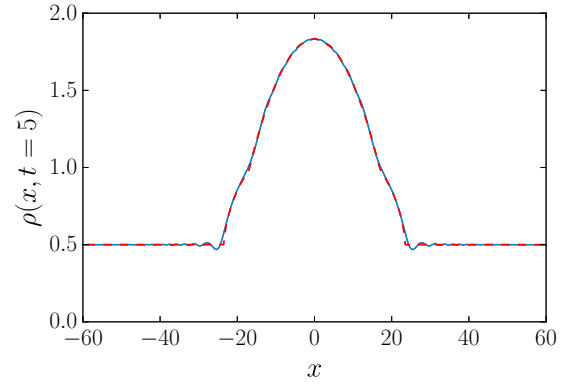


FIG. 6. Comparison between theory and simulations for $t = 5$. The red dashed curve is extracted from the exact solution of the dispersionless system (9) (see the text), while the blue curve displays the numerical solution of Eq. (2) with the initial conditions $u(x, 0) = 0$ and $\rho(x, 0)$ given by Eq. (3) taking $\rho_0 = 0.5$, $\rho_1 = 1.5$ (i.e., $\rho_m = 2$), and $x_0 = 20$. The corresponding initial distributions $\lambda^\pm(x, 0)$ are drawn schematically in Fig. 2(a), here with $c_0 = \sqrt{\rho_0} = \sqrt{0.5}$ and $c_m = \sqrt{\rho_m} = \sqrt{2}$.

by the very good agreement between theory and numerical simulations illustrated in Figs. 6 and 7. These figures, together with Fig. 8, compare at different times the theoretical density profile $\rho(x, t)$ with the one obtained by numerical integration of Eq. (2), taking the initial condition $u(x, 0) = 0$ and $\rho(x, 0)$ given by (3) with $\rho_0 = 0.5$, $\rho_m = 2$, and $x_0 = 20$. Similar agreement is obtained for the velocity profile $u(x, t)$. Note that for time $t = 5$, some small diffractive contributions at the left and right boundaries of the pulse are not accounted for by our dispersionless treatment (see Fig. 6). At larger time, the density profile at both ends of the pulse steepens and the amplitude of these oscillations accordingly increases. There exists a certain time, the wave breaking time t_{WB} , at which nonlinear spreading leads to a gradient catastrophe; the dispersionless approximation subsequently predicts a non-physical multivalued profile, as can be seen in Fig. 7 and more clearly in Fig. 8. The time t_{WB} can be easily computed if the wave breaking occurs at the simple-wave edges of the pulse (see, e.g., [47]) as it happens in our case, when the simple

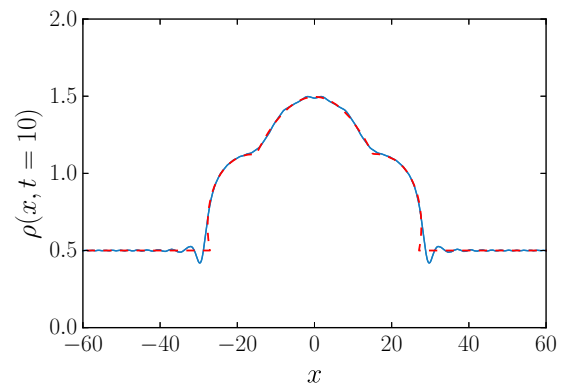


FIG. 7. Same as Fig. 6 but with $t = 10$. Notice that the dispersionless treatment leads to small regions of multivalued profile at both edges of the pulse.

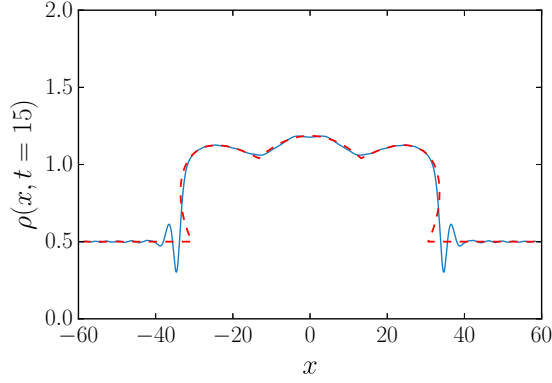


FIG. 8. Same as Figs. 6 and 7 but with $t = 15$. The multivaluedness of the theoretical profile is obvious here. It is associated with the formation of dispersive shocks at both edges of the pulse.

waves I and III break. These edges propagate with the sound velocity c_0 over a flat background and, at the wave breaking moment, the profile of λ^+ in region III (or λ^- in region I) has a vertical tangent line in the limit $\lambda^+ \rightarrow c_0$ ($\lambda^- \rightarrow -c_0$), that is, $\partial x / \partial \lambda^\pm \rightarrow 0$ as $\lambda^\pm \rightarrow \pm c_0$. Then differentiation of the simple-wave solution (39) or (40) gives at once

$$t_{\text{WB}} = \frac{2}{3} \left| \frac{dW_+^{(3)}(-c_0, \lambda^+)}{d\lambda^+} \right|_{\lambda^+=c_0} \quad (45)$$

(for definiteness we consider the simple wave in the region III). Substitution of the expression for $W_+^{(3)}(-c_0, \lambda^+)$ in the relation (45) yields, after simple calculations [48],

$$t_{\text{WB}} = \frac{2}{3} \left| \frac{dw^{\text{A}}}{d\lambda^+} \right|_{\lambda^+=c_0}. \quad (46)$$

The numerical value of t_{WB} is $\simeq 6.3$ for our choice of initial condition, in excellent agreement with the onset of double valuedness of the solution of the Euler-Poisson equation. In dispersive nonlinear systems the wave breaking is regularized by formation of regions with large oscillations of density and flow velocity, whose extent increases with time. This situation is typical for the formation of dispersive shock waves and requires a nonlinear treatment able to account for dispersive effects. Such an approach is introduced in the next section, but before turning to this aspect, we now compute an important characteristic time: the time t_{split} at which the initial bump has exactly split into two separated parts. For $t > t_{\text{split}}$ a plateau of constant density ρ_0 develops between the two separated humps, as illustrated, for instance, in Fig. 1. We can see from Fig. 4 that $t_{\text{split}} = t_{\text{SW}}(c_0)$ and can thus be computed from Eqs. (12) as

$$t_{\text{split}} = \frac{W_-^{(2)}(-c_0, c_0) - W_+^{(2)}(-c_0, c_0)}{v_+(-c_0, c_0) - v_-(-c_0, c_0)}. \quad (47)$$

On the right-hand side of this equation we have $W_\pm^{(2)} = \partial_\pm \chi^{(2)}$, where it is legitimate to use the expression (35) since we are in the limiting case where $\lambda^+ = -\lambda^-$. This yields at once

$$t_{\text{split}} = \frac{x_0}{c_0} + \frac{1}{4c_0^{5/2}} \int_{c_0}^{c_m} \sqrt{r} [w^{\text{A}}(r) - w^{\text{B}}(r)] dr. \quad (48)$$

In the limit of a very small initial bump, c_m is very close to c_0 and the second term on the right-hand side of Eq. (48) is negligible. In this case a linear approach is valid: The two subparts of the bump move, one to the right, the other to the left, at velocities $\pm c_0$ and a time $t_{\text{split}} \simeq x_0/c_0$ is needed for their complete separation. The second term on the right-hand side of Eq. (48) describes the nonlinear correction to this result. For the initial profile (3) the expressions of w^{A} and w^{B} are given in Eq. (18) and we directly obtain, from Eq. (48),

$$t_{\text{split}} = \frac{x_0}{c_0} [1 + G(\rho_1/\rho_0)], \quad (49)$$

where

$$G(X) = \frac{X}{4} \int_0^1 \frac{\sqrt{1-u}}{(1+Xu)^{1/4}} du. \quad (50)$$

In the simulations, we took $x_0 = 20$, $c_0 = \sqrt{0.5}$, and $\rho_1/\rho_0 = 3$ and formula (49) then yields $t_{\text{split}} \simeq 40.1$. Note that in this case the simple linear estimate would be $x_0/c_0 \simeq 28.3$. The accuracy of the result (49) can be checked against numerical simulations by plotting the numerically determined central density of the hump $\rho(x=0, t)$ as a function of time and checking that it just reaches the background value at $t = t_{\text{split}}$. This is indeed the case: For the case we consider here $\rho(x=0, t=40.1)$ departs from ρ_0 by only 3%.

For a small bump with $\rho_1 \ll \rho_0$, the weak nonlinear correction to the linear result is obtained by evaluating the small- X behavior of the function G in (50). This yields

$$t_{\text{split}} \simeq \frac{x_0}{c_0} \left[1 + \frac{1}{6} \frac{\rho_1}{\rho_0} - \frac{1}{60} \left(\frac{\rho_1}{\rho_0} \right)^2 + \dots \right]. \quad (51)$$

For the numerical values for which we performed the simulations, stopping expansion (51) at first order in ρ_1/ρ_0 yields $t_{\text{split}} \simeq 42.4$. At the next order we get $t_{\text{split}} \simeq 38.2$. These values are reasonable upper and lower bounds for the exact result. Of course, the expansion is more efficient for lower values of ρ_1/ρ_0 : Even for the relatively large value $\rho_1/\rho_0 = 1$, expansion (51) gives an estimate which is off the exact result (49) by only 0.3%.

IV. WHITHAM THEORY AND GENERALIZED HODOGRAPH METHOD

In this section we first give a general presentation of Whitham modulational theory (Sec. IV A) and then discuss specific features of its implementation for the case in which we are interested (Sec. IV B).

A. Periodic solutions and their modulations

The NLS equation (2) is equivalent to the system (6) which admits nonlinear periodic solutions that can be written in terms of four parameters $\lambda_1 \leq \lambda_2 \leq \lambda_3 \leq \lambda_4$ in the form (see, e.g., Ref. [43])

$$\begin{aligned} \rho(x, t) &= \frac{1}{4} (\lambda_4 - \lambda_3 - \lambda_2 + \lambda_1)^2 + (\lambda_4 - \lambda_3)(\lambda_2 - \lambda_1) \\ &\quad \times \text{sn}^2(\sqrt{(\lambda_4 - \lambda_2)(\lambda_3 - \lambda_1)}(x - Vt), m), \\ u(x, t) &= V - \frac{C}{\rho(x, t)}, \end{aligned} \quad (52)$$

where sn is the Jacobi elliptic sine function (see, e.g., Ref. [46]),

$$V = \frac{1}{2} \sum_{i=1}^4 \lambda_i, \quad m = \frac{(\lambda_2 - \lambda_1)(\lambda_4 - \lambda_3)}{(\lambda_4 - \lambda_2)(\lambda_3 - \lambda_1)}, \quad (53)$$

and

$$C = \frac{1}{8}(-\lambda_1 - \lambda_2 + \lambda_3 + \lambda_4)(-\lambda_1 + \lambda_2 - \lambda_3 + \lambda_4) \times (\lambda_1 - \lambda_2 - \lambda_3 + \lambda_4). \quad (54)$$

For constant λ_i , expressions (52)–(54) correspond to an exact (single-phase) solution of the NLS equation, periodic in time and space, where oscillations have the amplitude

$$a = (\lambda_2 - \lambda_1)(\lambda_4 - \lambda_3) \quad (55)$$

and the spatial wavelength

$$L = \frac{2\mathbf{K}(m)}{\sqrt{(\lambda_4 - \lambda_2)(\lambda_3 - \lambda_1)}}. \quad (56)$$

In the limit $m \rightarrow 0$ ($\lambda_1 = \lambda_2$ or $\lambda_3 = \lambda_4$), $\text{sn}(x, m) \rightarrow \sin(x)$ and Eq. (52) describes a small-amplitude sinusoidal wave oscillating around a constant background. In the other limiting case $m \rightarrow 1$ ($\lambda_2 = \lambda_3$), $\text{sn}(x, m) \rightarrow \tanh(x)$ and Eq. (52) describes a dark soliton (for which $L \rightarrow \infty$).

The great insight of Gurevich and Pitaevskii [34] was to describe a dispersive shock wave as a slowly modulated nonlinear wave, of type (52), for which the λ_i are functions of x and t which vary weakly over one wavelength and one period. Their slow evolution is governed by the Whitham equations [30,43]

$$\partial_t \lambda_i + v_i(\lambda_1, \lambda_2, \lambda_3, \lambda_4) \partial_x \lambda_i = 0, \quad i = 1, 2, 3, 4. \quad (57)$$

Comparing with Eqs. (9), we see that the λ_i are the Riemann invariants of the Whitham equations first found in Refs. [49,50]. The v_i are the associated characteristic velocities; their explicit expressions can be obtained from the relation [38,43]

$$v_i = V - \frac{1}{2} \frac{L}{\partial_i L}, \quad i = 1, 2, 3, 4, \quad (58)$$

where $\partial_i = \partial/\partial\lambda_i$. This yields

$$\begin{aligned} v_1 &= V - \frac{(\lambda_4 - \lambda_1)(\lambda_2 - \lambda_1)\mathbf{K}(m)}{(\lambda_4 - \lambda_1)\mathbf{K}(m) - (\lambda_4 - \lambda_2)\mathbf{E}(m)}, \\ v_2 &= V + \frac{(\lambda_3 - \lambda_2)(\lambda_2 - \lambda_1)\mathbf{K}(m)}{(\lambda_3 - \lambda_2)\mathbf{K}(m) - (\lambda_3 - \lambda_1)\mathbf{E}(m)}, \\ v_3 &= V - \frac{(\lambda_4 - \lambda_3)(\lambda_3 - \lambda_2)\mathbf{K}(m)}{(\lambda_3 - \lambda_2)\mathbf{K}(m) - (\lambda_4 - \lambda_2)\mathbf{E}(m)}, \\ v_4 &= V + \frac{(\lambda_4 - \lambda_3)(\lambda_4 - \lambda_1)\mathbf{K}(m)}{(\lambda_4 - \lambda_1)\mathbf{K}(m) - (\lambda_3 - \lambda_1)\mathbf{E}(m)}, \end{aligned} \quad (59)$$

where m is given by Eq. (53) and $\mathbf{E}(m)$ is the complete elliptic integrals of the second kind.

In the soliton limit $m \rightarrow 1$, i.e., $\lambda_3 \rightarrow \lambda_2$, the Whitham velocities reduce to

$$\begin{aligned} v_1 &= \frac{1}{2}(3\lambda_1 + \lambda_4), & v_2 = v_3 &= \frac{1}{2}(\lambda_1 + 2\lambda_2 + \lambda_4), \\ v_4 &= \frac{1}{2}(\lambda_1 + 3\lambda_4). \end{aligned} \quad (60)$$

In a similar way, in the small-amplitude limit $m \rightarrow 0$, i.e., $\lambda_2 \rightarrow \lambda_1$, we obtain

$$\begin{aligned} v_1 = v_2 &= 2\lambda_1 + \frac{(\lambda_4 - \lambda_3)^2}{2(\lambda_3 + \lambda_4 - 2\lambda_1)}, \\ v_3 &= \frac{1}{2}(3\lambda_3 + \lambda_4), & v_4 &= \frac{1}{2}(\lambda_3 + 3\lambda_4), \end{aligned} \quad (61)$$

and in another small-amplitude limit ($m \rightarrow 0$ when $\lambda_3 \rightarrow \lambda_4$), we have

$$\begin{aligned} v_1 &= \frac{1}{2}(3\lambda_1 + \lambda_2), & v_2 &= \frac{1}{2}(\lambda_1 + 3\lambda_2), \\ v_3 = v_4 &= 2\lambda_4 + \frac{(\lambda_2 - \lambda_1)^2}{2(\lambda_1 + \lambda_2 - 2\lambda_4)}. \end{aligned} \quad (62)$$

B. Generalized hodograph method

In Sec. III we have provided a nondispersive description of the spreading and splitting of the initial pulse in two parts (one propagating to the left and the other to the right). During this nonlinear process the leading wavefront steepens and leads to wave breaking. This occurs at a certain time t_{WB} after which the approach of Sec. III predicts a nonphysical multivalued profile (see, e.g., Fig. 8), since it does not take into account dispersive effects. The process of dispersive regularization of the gradient catastrophe leads to the formation of a dispersive shock wave, as first predicted by Sagdeev in the context of collisionless plasma physics (see, e.g., Ref. [51]).

For the specific case we are interested in, the Gurevich-Pitaevskii approach, which consists in using Whitham theory for describing the DSW as a slowly modulated nonlinear wave, holds, but it is complicated by the fact that two of the four Riemann invariants vary in the shock region. As already explained in the Introduction, we adapt here the method developed in Refs. [37–40] for treating a similar situation for the Korteweg–de Vries equation. The general case of NLS dispersive shock with all four Riemann invariants varying was considered in Ref. [52].

In all the following we concentrate our attention on the shock formed at the right edge of the pulse propagating to the right. Due to the symmetry of the problem, the same treatment can be employed for the left pulse. The prediction of multivalued λ^+ resulting from the dispersionless approach of Sec. III suggests that after wave breaking of the simple-wave solution, the correct Whitham-Riemann invariant should be sought in a configuration such that $\lambda_1 = \lambda^- = -c_0$, $\lambda_2 = \lambda^+(x \rightarrow \infty) = c_0$, and λ_3 and λ_4 both depend on x and t . In this case the Whitham equations (57) with $i = 1, 2$ are trivially satisfied, and to solve them for $i = 3$ and 4, we introduce two functions $W_i(\lambda_3, \lambda_4)$ ($i = 3$ or 4), exactly as we did in Sec. III with $W_{\pm}(\lambda^-, \lambda^+)$:

$$x - v_i(\lambda_3, \lambda_4)t = W_i(\lambda_3, \lambda_4), \quad i = 3, 4. \quad (63)$$

For the sake of brevity we have defined in this equation $v_i(\lambda_3, \lambda_4) = v_i(\lambda_1 = -c_0, \lambda_2 = c_0, \lambda_3, \lambda_4)$ for $i \in \{3, 4\}$; we will keep this notation henceforth.

Then we can derive Tsarev equations for $W_i(\lambda_3, \lambda_4)$ [replacing the subscripts $+$ and $-$ by 4 and 3 in (13)] and we can show (see, e.g., Refs. [38,52–54]) that these are solved for W_i

of the form

$$W_i = \left(1 - \frac{L}{\partial_i L} \partial_i\right) \mathscr{W} = \mathscr{W} + 2(v_i - V) \partial_i \mathscr{W}, \quad (64)$$

where $\mathscr{W}(\lambda_3, \lambda_4)$ is solution of the Euler-Poisson equation

$$\partial_{34} \mathscr{W} = \frac{\partial_3 \mathscr{W} - \partial_4 \mathscr{W}}{2(\lambda_3 - \lambda_4)}. \quad (65)$$

As was first understood in Ref. [36], after the wave breaking time, the development of the dispersive shock wave occurs in *two* steps. Initially (when t is close to t_{WB}), the DSW is connected at its left edge to the smooth profile coming from the time evolution of the right part of the initial profile of λ^+ (part A), which is gradually absorbed in the DSW. This process of absorption is complete at a time we denote by $t_{A|B}$. Then, for $t > t_{A|B}$, the DSW is connected to the smooth profile coming from the time evolution of part B of λ^+ [this is case B, region B of the (x, t) plane]. During the initial step (for $t < t_{A|B}$), for a given time t , the highest value of the largest Riemann invariant is reached within the smooth part of the profile and keeps the constant value c_m . Then, in the subsequent time evolution, this highest value is reached within the DSW (or at its right boundary) where there exists a point where λ_4 takes its maximal value (c_m). We illustrate these two steps of development of the DSW in Fig. 9. We refer to the region of the DSW where λ_4 is a decreasing function of x as region A and the part where it increases as region B.

In region A of the (x, t) plane, we denote by $\mathscr{W}^A(\lambda_3, \lambda_4)$ the solution of the Euler-Poisson equation and in region B we denote it instead by $\mathscr{W}^B(\lambda_3, \lambda_4)$. These two forms are joined by the line $\lambda_4 = c_m$, where

$$\mathscr{W}^A(\lambda_3, c_m) = \mathscr{W}^B(\lambda_3, c_m). \quad (66)$$

We denote the position where this matching condition is realized by $x_m(t)$ [see Fig. 9(b)]. The corresponding boundary in the (x, t) plane is represented as a green solid curve in Fig. 10.

Since the general solution of the Euler-Poisson equation with the appropriate boundary conditions and the construction of the resulting nonlinear pattern are quite involved, we will first consider some particular but useful results which follow from general principles of the Whitham theory.

V. MOTION OF THE SOLITON EDGE OF THE SHOCK

During the first stage of evolution of the DSW, its left (solitonic) edge is connected to the smooth dispersionless solution whose dynamics is described by formula (39), that is, we have here

$$x_S - v_+(-c_0, \lambda_S)t = W_+^{(3)}(-c_0, \lambda_S), \quad (67)$$

where $x_S(t)$ is the position of the left edge of the DSW and $\lambda_S(t) \equiv \lambda^+(x_S(t), t)$. We recall that in all the following we focus on the DSW formed in the right part of the pulse. Hence Eq. (67) concerns the right part of the nondispersive part of the profile. According to the terminology of Sec. III, this corresponds to region III.

On the other hand, in vicinity of this boundary, the Whitham equations (57) with the limiting expressions (60)

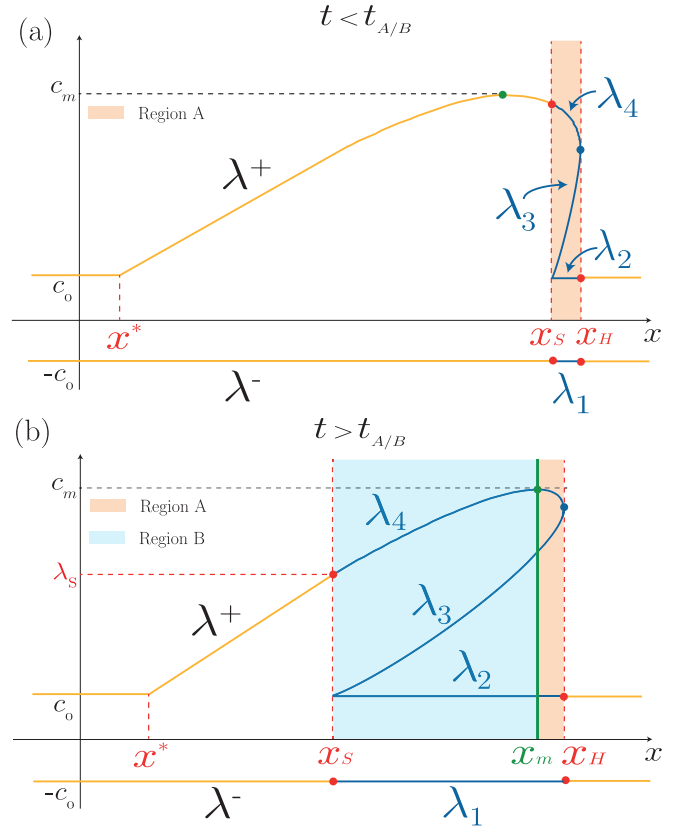


FIG. 9. Schematic plots of the position dependence of the Riemann invariants inside (blue solid curves) and outside (yellow solid curves) the DSW (colored region). (a) For $t < t_{A|B}$, the DSW is connected to the smooth profile coming from the time evolution of part A of the initial pulse. At $t = t_{A|B}$, part A is completely absorbed by the DSW. Thus, for this time, the shock wave connects to the smooth profile exactly at $\lambda_+(x_S(t), t) = c_m$. (b) For $t > t_{A|B}$, the DSW is connected at its left edge at a point belonging to part B of the dispersionless profile. In this case the shock wave is divided into two regions A and B, separated by the green vertical line in the plot. The continuity along the separation line between the two regions, i.e., at $x = x_m(t)$, is ensured by Eq. (66).

(where $\lambda_2 = \lambda_3 = c_0$) for the velocities v_i are given by

$$\begin{aligned} \partial_t \lambda_3 + \frac{1}{2}(\lambda_4 + c_0) \partial_x \lambda_3 &= 0, \\ \partial_t \lambda_4 + \frac{1}{2}(3\lambda_4 - c_0) \partial_x \lambda_4 &= 0. \end{aligned} \quad (68)$$

To solve these equations we can perform a classical hodograph transform, that is, we assume that x and t are functions of the independent variables λ_3 and λ_4 : $t = t(\lambda_3, \lambda_4)$ and $x = x(\lambda_3, \lambda_4)$. We find from Eqs. (68) that these functions must satisfy the linear system

$$\begin{aligned} \frac{\partial x}{\partial \lambda_3} - \frac{1}{2}(3\lambda_4 - c_0) \frac{\partial t}{\partial \lambda_3} &= 0, \\ \frac{\partial x}{\partial \lambda_4} - \frac{1}{2}(\lambda_4 + c_0) \frac{\partial t}{\partial \lambda_4} &= 0. \end{aligned}$$

At the left edge of the DSW, the second equation reads

$$\frac{\partial x_S}{\partial \lambda_S} - \frac{1}{2}(\lambda_S + c_0) \frac{\partial t}{\partial \lambda_S} = 0, \quad (69)$$

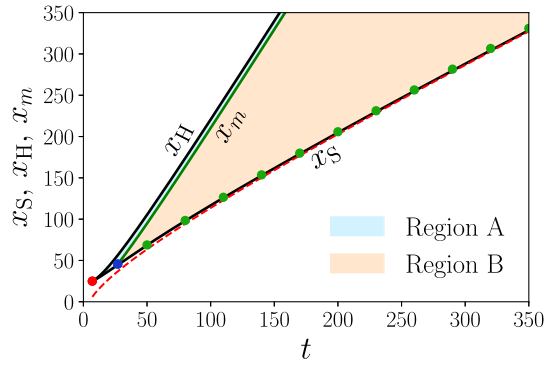


FIG. 10. Black solid curves show the time evolution of $x_S(t)$ and $x_H(t)$ calculated from Eqs. (96) and (99), respectively. The green solid curve shows the time evolution of $x_m(t)$, for which $\lambda_4(x_m(t), t) = c_m$, which marks the separation between regions A and B. The red dashed curve shows the asymptotic behavior of $x_S(t)$, from Eq. (81). The green points indicate the positions $x_S(t)$ extracted from simulations, for an initial condition (3) with $\rho_0 = 0.5$, $\rho_m = 2$, and $x_0 = 20$. The red point marks the birth of the DSW (at time $t_{WB} \simeq 6.3$), while the blue one initiates region B (at time $t_{A|B} \simeq 25.9$).

which must be compatible with Eq. (67). Differentiation of Eq. (67) with respect to λ_S and elimination of $\partial x_S / \partial \lambda_S$ with the use of Eq. (69) yields a differential equation for the function $t(\lambda_S) \equiv t(c_0, \lambda_S)$:

$$(\lambda_S - c_0) \frac{dt}{d\lambda_S} + \frac{3}{2}t = -\frac{dW_+^{(3)}(-c_0, \lambda_S)}{d\lambda_S}. \quad (70)$$

At the wave breaking time, $\lambda_S = c_0$, which corresponds to the definition $t_{WB} = t(c_0)$, and Eq. (70) then yields

$$t_{WB} = -\frac{2}{3} \left. \frac{dW_+^{(3)}(-c_0, \lambda_S)}{d\lambda_S} \right|_{\lambda_S=c_0}, \quad (71)$$

in agreement with Eq. (46), which should be expected since at the wave breaking moment the DSW reduces to a point in the Whitham approximation. For the concrete case of our initial distribution we can get a simple explicit expression for t_{WB} which reads [see Eq. (46) and note [48]]

$$t_{WB} = -\frac{2}{3} \left. \frac{dw^A(\lambda_S)}{d\lambda_S} \right|_{\lambda_S=c_0} = \frac{2c_0x_0}{3\rho_1}, \quad (72)$$

where the right-hand side is the form of the central formula corresponding to the initial profile (3). Taking $\rho_0 = 0.5$, $\rho_m = 2$, and $x_0 = 20$, we find $t_{WB} \simeq 6.3$, in excellent agreement with the numerical simulations.

The solution of Eq. (70) reads

$$\begin{aligned} t(\lambda_S) &= \frac{-1}{(\lambda_S - c_0)^{3/2}} \int_{c_0}^{\lambda_S} \sqrt{r - c_0} \frac{dW_+^{(3)}(-c_0, r)}{dr} dr \\ &= \frac{1}{2(\lambda_S - c_0)^{3/2}} \int_{c_0}^{\lambda_S} \frac{W_+^{(3)}(-c_0, r)}{\sqrt{r - c_0}} dr \\ &\quad - \frac{W_+^{(3)}(-c_0, \lambda_S)}{\lambda_S - c_0}. \end{aligned} \quad (73)$$

Substituting this expression into (67), we obtain the function $x_S(\lambda_S) \equiv x(c_0, \lambda_S)$:

$$x_S(\lambda_S) = \frac{1}{2}(3\lambda_S - c_0)t(\lambda_S) + W_+^{(3)}(-c_0, \lambda_S). \quad (74)$$

The two formulas (73) and (74) define, in an implicit way, the law of motion $x = x_S(t)$ of the soliton edge of the DSW.

The above expressions are correct as long as the soliton edge is located inside region A of the DSW, that is, up to the moment $t_{A|B} = t(c_m)$. From (73) we obtain the explicit expression

$$t_{A|B} = \frac{-1}{(c_m - c_0)^{3/2}} \int_{c_0}^{c_m} \sqrt{r - c_0} \frac{dW_+^{(3)}(-c_0, r)}{dr} dr. \quad (75)$$

In the case we consider, this yields $t_{A|B} = 25.9$. For time larger than $t_{A|B}$ the soliton edge connects with region B of the dispersionless profile, which corresponds to region Π_r (see Fig. 4). Concretely, for a time $t > t_{A|B}$, instead of Eq. (70) we have to solve the differential equation

$$(\lambda_S - c_0) \frac{dt}{d\lambda_S} + \frac{3}{2}t = -\frac{dW_+^{(2)}(-c_0, \lambda_S)}{d\lambda_S}, \quad (76)$$

with the initial condition $t(c_m) = t_{A|B}$. The solution of Eq. (76) reads

$$\begin{aligned} t(\lambda_S) &= \frac{-1}{(\lambda_S - c_0)^{3/2}} \left(\int_{c_m}^{\lambda_S} \sqrt{r - c_0} \frac{dW_+^{(2)}(-c_0, r)}{dr} dr \right. \\ &\quad \left. + \int_{c_0}^{c_m} \sqrt{r - c_0} \frac{dW_+^{(3)}(-c_0, r)}{dr} dr \right) \end{aligned} \quad (77)$$

and $x_S(\lambda_S)$ is determined by Eq. (41):

$$x_S(\lambda_S) = \frac{1}{2}(3\lambda_S - c_0)t(\lambda_S) + W_+^{(2)}(-c_0, \lambda_S). \quad (78)$$

At asymptotically large time $t \rightarrow \infty$ we are in stage B of evolution of the DSW with furthermore $\lambda_S \rightarrow c_0$. In this case the upper limit of integration in the first integral of formula (77) can be set equal to c_0 . Thus, we get in this limit

$$t(\lambda_S) \simeq \frac{\mathcal{A}}{(\lambda_S - c_0)^{3/2}}, \quad (79)$$

where the expression for the constant \mathcal{A} is

$$\begin{aligned} \mathcal{A} &= -\left(\int_{c_m}^{c_0} \sqrt{r - c_0} \frac{dW_+^{(2)}(-c_0, r)}{dr} dr \right. \\ &\quad \left. + \int_{c_0}^{c_m} \sqrt{r - c_0} \frac{dW_+^{(3)}(-c_0, r)}{dr} dr \right). \end{aligned} \quad (80)$$

Consequently, we obtain the asymptotic expressions

$$\lambda_S(t) = c_0 + \left(\frac{\mathcal{A}}{t} \right)^{2/3}, \quad x_S(t) = c_0 t + \frac{3\mathcal{A}^{2/3}}{2} t^{1/3}. \quad (81)$$

We denote the position of the rear point of the simple wave by $x^*(t)$ (see Fig. 9). It is clear from Fig. 4 that $x^* = 0$ at time $t = t_{SW}(c_0)$, i.e., just when region 2 disappears, whereafter the dispersionless approach of Sec. III predicts a profile with only simple waves and plateau regions. The rear edge of the simple wave then propagates over a flat background at constant velocity c_0 ; we thus have

$$x^*(t) = c_0[t - t_{SW}(c_0)]. \quad (82)$$

Asymptotically, i.e., at time much larger than $t_{\text{SW}}(c_0)$, we have $x^*(t) \simeq c_0 t$ and, in the simple-wave profile between $x^*(t)$ and $x_S(t)$, λ^+ depends on the self-similar variable $[x - x^*(t)]/t$ while λ^- is constant. Then Eqs. (9) readily yield

$$\lambda^+ = c_0 + \frac{2}{3} \frac{x - x^*(t)}{t}, \quad \lambda^- = -c_0 \quad \text{for } x \in [x^*(t), x_S(t)]. \quad (83)$$

Equation (8) then yields the explicit expression of ρ in this region (which was roughly described at the end of Sec. II as having a quasitriangular shape), and using (81) we obtain

$$\int_{x^*(t)}^{x_S(t)} [\sqrt{\rho(x, t)} - c_0]^{1/2} dx = \frac{1}{\sqrt{2}} \mathcal{A}. \quad (84)$$

The asymptotic situation at the rear of the DSW is reminiscent of what occurs in the theory of weak dissipative shocks where (i) a nonlinear pattern of triangular shape may also appear at the rear edge of a (viscous) shock, (ii) the details of the initial distribution are lost at large time (as in the present case), and (iii) a conserved quantity of the type (84) also exists. Hence the above results provide, for a conservative system, the counterpart of the weak viscous shock theory (presented, for instance, in Ref. [30]). Note, however, that the boundary conditions at the large-amplitude edge of the shock are different depending on whether we consider a dissipative or a conservative system and that the corresponding velocity and conserved quantity are accordingly also different. Note also that equivalent relations for the behavior of a rarefaction wave in the rear of a dispersive shock in the similar situation for the Korteweg–de Vries equation have been obtained in Ref. [31].

Formulas (81) and (84) are important because they provide indirect evidence making it possible to assert if a given experiment has indeed reached the point where a bona fide dispersive shock wave should be expected.

In the next section we give an explicit theoretical description of the whole region of the dispersive shock.

VI. SOLUTION IN THE SHOCK REGION

In this section we turn to the general solution of the Whitham equations given by the formulas of Sec. IV B. Our task is to express the functions W_3 and W_4 in terms of the initial distribution of the light pulse. As was indicated above, we need to distinguish two regions, A and B, in which \mathcal{W} takes different values.

A. Solution in region A

In region A we can straightforwardly adapt the procedure explained in Ref. [38]. We impose the matching of the left edge of the DSW with the dispersionless solution (see Sec. III B): Just at $x = x_S(t)$, we have $\lambda_4 = \lambda^+$, $\lambda_3 = \lambda_2 = c_0$, and $\lambda_1 = -c_0$ (see Fig. 9) and Eq. (60) yields $v_4(\lambda_3, \lambda_4) = (3\lambda_4 - c_0)/2 = v_+(-c_0, \lambda^+)$. Then, at this point, the conditions (39) and (63) with $i = 4$ are simultaneously satisfied, which implies

$$W_4^A(\lambda_3 = c_0, \lambda_4 = \lambda^+) = W_+^{(3)}(-c_0, \lambda^+), \quad (85)$$

where $W_+^{(3)}$ is the form of W_+ corresponding to region 3. Note that here the first argument of the function $W_+^{(3)}$ is $\lambda^- = -c_0$ for all times. Indeed, the boundary condition (85) corresponds to the matching in physical space at $x_S(t)$. When the DSW starts to form at time t_{WB} , the edge $x_S(t_{\text{WB}})$ lies on the characteristic issued from x_0 [x_0 defines the initial extent of the pulse; see Eq. (3)]. The Riemann invariant λ^- is constant and equal to $-c_0$ along this characteristic (cf. Fig. 4). Then, because the characteristics of λ^- in the dispersionless region close to x_S are oriented to the left whereas x_S moves to the right, it is clear that $\lambda^-(x_S(t), t) = -c_0$ for $t \geq t_{\text{WB}}$.

In terms of \mathcal{W} the relation (85) corresponds to the equation

$$\mathcal{W}^A(c_0, \lambda_4) + 2(\lambda_4 - c_0)\partial_4 \mathcal{W}^A(c_0, \lambda_4) = W_+^{(3)}(-c_0, \lambda_4), \quad (86)$$

whose solution is

$$\mathcal{W}^A(c_0, \lambda_4) = \frac{1}{2\sqrt{\lambda_4 - c_0}} \int_{c_0}^{\lambda_4} \frac{W_+^{(3)}(-c_0, r) dr}{\sqrt{r - c_0}}. \quad (87)$$

This will serve as a boundary condition for the Euler-Poisson equation (65) whose general solution has been given by Eisenhart [55] in the form

$$\mathcal{W}^A(\lambda_3, \lambda_4) = \int_{c_0}^{\lambda_3} \frac{\psi^A(\mu) d\mu}{\sqrt{\lambda_3 - \mu} \sqrt{\lambda_4 - \mu}} + \int_{c_0}^{\lambda_4} \frac{\varphi^A(\mu) d\mu}{\sqrt{|\lambda_3 - \mu|} \sqrt{\lambda_4 - \mu}}, \quad (88)$$

where $\varphi^A(\mu)$ and $\psi^A(\mu)$ are arbitrary functions to be determined from the appropriate boundary conditions. By taking $\lambda_3 = c_0$ in this expression we see that $\varphi^A(\mu)/\sqrt{\mu - c_0}$ is the Abel transform of $\mathcal{W}^A(c_0, \lambda_4)$. Using the inverse transformation [56] and expression (87) we can show that

$$\varphi^A(\mu) = \frac{1}{2\pi\sqrt{\mu - c_0}} \int_{c_0}^{\mu} \frac{W_+^{(3)}(-c_0, r) dr}{\sqrt{\mu - r}}, \quad (89)$$

where we recall that $W_+^{(3)} = \partial_+ \chi^{(3)}$. In order to determine the other unknown function ψ^A , we consider the right boundary of the DSW where λ_3 and λ_4 are asymptotically close to each other. We can show (see, e.g., equivalent reasoning in Ref. [31]) that in order to avoid divergence of $\mathcal{W}^A(\lambda_3, \lambda_4 = \lambda_3)$, we need to impose $\psi^A(\lambda) = -\varphi^A(\lambda)$. The final form of the Eisenhart solution in region A thus reads

$$\mathcal{W}^A(\lambda_3, \lambda_4) = \int_{\lambda_3}^{\lambda_4} \frac{\varphi^A(\mu) d\mu}{\sqrt{\mu - \lambda_3} \sqrt{\lambda_4 - \mu}}, \quad (90)$$

where φ^A is given by formula (89).

B. Solution in region B

We look for a solution of the Euler-Poisson equation in region B in the form

$$\mathcal{W}^B(\lambda_3, \lambda_4) = \mathcal{W}^A(\lambda_3, \lambda_4) + \int_{\lambda_4}^{c_m} \frac{\varphi^B(\mu) d\mu}{\sqrt{\mu - \lambda_3} \sqrt{\mu - \lambda_4}}, \quad (91)$$

where c_m is the maximum value for λ_4 . This expression ensures that \mathcal{W}^B , (i) being the sum of two solutions of the

Euler-Poisson equation, is also a solution of this equation and (ii) verifies the boundary condition (66) since the second term on the right-hand side of (91) vanishes when $\lambda_4 = c_m$.

At the left boundary of the DSW, $\mathscr{W}^B(c_0, \lambda_4)$ verifies an equation similar to (86):

$$\mathscr{W}^B(c_0, \lambda_4) + 2(\lambda_4 - c_0)\partial_4 \mathscr{W}^B(c_0, \lambda_4) = W_+^{(2)}(-c_0, \lambda_4). \quad (92)$$

The solution with the appropriate integration constant reads

$$\begin{aligned} \mathscr{W}^B(r_1, 0) &= \frac{1}{2\sqrt{\lambda_4 - c_0}} \int_{\lambda_4}^{c_m} \frac{W_+^{(2)}(-c_0, r)}{\sqrt{r - c_0}} dr \\ &+ \frac{1}{2\sqrt{\lambda_4 - c_0}} \int_{c_0}^{c_m} \frac{W_+^{(3)}(-c_0, r)}{\sqrt{r - c_0}} dr, \end{aligned} \quad (93)$$

where $W_+^{(2)}$ is the form of W_+ corresponding to region 2. The same procedure as the one previously used for region A of the DSW leads here to

$$\varphi^B(\mu) = \frac{1}{2\pi\sqrt{\mu - c_0}} \int_{\mu}^{c_m} \frac{W_+^{(3)}(-c_0, r) - W_+^{(2)}(-c_0, r)}{\sqrt{\mu - r}} dr. \quad (94)$$

Equations (91) and (94) give the solution of the Euler-Poisson equation in region B.

C. Characteristics of the DSW at its edges

It is important to determine the boundaries $x_S(t)$ and $x_H(t)$ of the DSW, as well as the values of the Riemann invariants λ_3 and λ_4 at these points. The law of motion of the soliton edge was already found in Sec. V and it is instructive to show how this result can be obtained from the general solution.

At the soliton edge we have $\lambda_2 = \lambda_3 = c_0$ and $\lambda_4 = \lambda_S(t)$. The corresponding Whitham velocities are $v_3 = (\lambda_S + c_0)/2$ and $v_4 = (3\lambda_S - c_0)/2$ [see Eqs. (60)], and Eqs. (63) read

$$\begin{aligned} x_S - \frac{1}{2}(3\lambda_S - c_0)t &= W_4^\alpha(c_0, \lambda_S) = W_+^{(n)}(-c_0, \lambda_S), \\ x_S - \frac{1}{2}(\lambda_S + c_0)t &= W_3^\alpha(c_0, \lambda_S) = \mathscr{W}^\alpha(c_0, \lambda_S), \end{aligned} \quad (95)$$

where, in order to have formulas applying to both stages of evolution of the DSW, we have introduced dummy indices α and n with $\alpha = A$ or B and $n = 3$ or 2 , respectively. This gives at once

$$\begin{aligned} t(\lambda_S) &= \frac{1}{\lambda_S - c_0} [\mathscr{W}^\alpha(c_0, \lambda_S) - W_+^{(n)}(-c_0, \lambda_S)], \\ x_S(\lambda_S) &= c_0 t + \frac{1}{2} [3\mathscr{W}^\alpha(c_0, \lambda_S) - W_+^{(n)}(-c_0, \lambda_S)]. \end{aligned} \quad (96)$$

Let us consider stage A, for instance. Equation (87) yields

$$\mathscr{W}^A(c_0, \lambda_S) = \frac{1}{2\sqrt{\lambda_S - c_0}} \int_{c_0}^{\lambda_S} \frac{W_+^{(3)}(-c_0, r)}{\sqrt{r - c_0}} dr,$$

which inserted into Eqs. (96) gives immediately the results (73) and (74).

Figure 10 shows the time evolution of $x_S(t)$. The black curve is calculated from Eqs. (96), while the red dashed curve corresponds to the asymptotic behavior of x_S , given by Eq. (81). The green points are extracted from simulations and exhibit very good agreement with the theory. The same

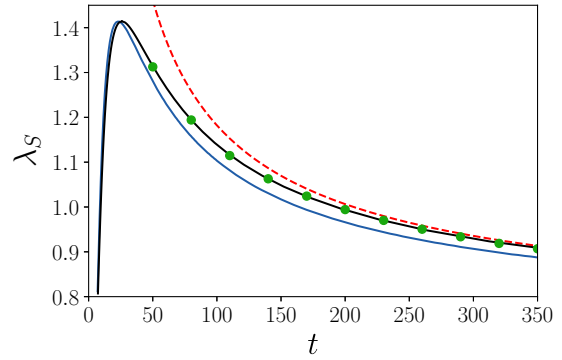


FIG. 11. The black solid curve shows the time evolution of $\lambda_S(t)$ from Eq. (96), or equivalently from Eq. (73) and then (77). The red dashed curve shows the asymptotic behavior from Eq. (81). The green points are extracted from simulations for different times, for the initial profile (3) with $\rho_0 = 0.5$, $\rho_m = 2$, and $x_0 = 20$. The blue solid curve is an approximation obtained by schematically describing the initial splitting by assuming $\lambda^- \simeq \text{const}$ for all t during the evolution of the right pulse (see the text).

excellent agreement is obtained for the time evolution of λ_S , as shown in Fig. 11.

We demonstrated in Sec. III the accuracy of the Riemann method for describing the spreading and splitting of the initial pulse into two parts. The matching between the left edge of the DSW and the dispersionless profile at the point of coordinates (x_S, λ_S) is given in Eq. (67). Since the splitting occurs rapidly, a simpler approach would be to make the approximation $\lambda^-(x, t) = -c_0 = \text{const}$ for the dispersionless right part of the profile. In this case, the Riemann equation (9) for λ^+ reduces to

$$\frac{\partial \lambda^+}{\partial t} + \left(\frac{3}{2} \lambda^+ - \frac{1}{2} c_0 \right) \frac{\partial \lambda^+}{\partial x} = 0. \quad (97)$$

This equation can be solved by the method of characteristics, which yields the implicit solution for $\lambda^+(x, t)$,

$$x - \left(\frac{3}{2} \lambda^+ - \frac{1}{2} c_0 \right) t = w^{A(B)}(\lambda^+), \quad (98)$$

where $w^{A(B)}$ is the inverse function of the initial $\lambda^+(x)$ profile in part A (B) [in our case the explicit expressions are given in Eqs. (18)].

Within this approximation the DSW is described through \mathscr{W} by the same equations (89)–(91) and (94) as before, replacing $W_+^{(3/2)}(-c_0, r)$ by $w^{A(B)}(r)$ everywhere. Further, λ_S computed using this approximation is represented in Fig. 11 as a function of t (blue solid curve), where it is also compared with the results obtained using the full Riemann method (black solid curve) and the results extracted from numerical simulations (green points). As we can see, an accurate description of the spreading and splitting stage is important since the blue curve does not precisely agree with the results of the simulations, mainly at large times. However, this approximation gives a correct description of the initial formation of the DSW: This is discussed in Ref. [48], where it is argued that, close to the wave breaking time, the approximation $W_+^{(3)}(-c_0, r) \simeq w^A(r)$ is very accurate.

Let us now turn to the determination of the location $x_H(t)$ of the small-amplitude harmonic boundary of the DSW and of

the common value $\lambda_H(t)$ of λ_3 and λ_4 at this point (see Fig. 9). In the typical situation the left boundary is located in region A. In this case the equations (63) for $i = 3$ and 4 are equivalent and read

$$x_H - v_H t = W_i^A(\lambda_H, \lambda_H), \quad i = 3 \text{ or } 4, \quad (99)$$

where $v_H = v_i(\lambda_H, \lambda_H) = 2\lambda_H - c_0^2/\lambda_H$ [cf. Eqs. (62)]. An equation for λ_H alone is obtained by demanding that the velocity dx_H/dt of the left boundary is equal to the common value v_H of v_3 and v_4 . The differentiation of Eq. (99) with respect to time then yields

$$t = -\frac{1}{dv_H/d\lambda_H} \frac{dW_4^A(\lambda_H, \lambda_H)}{d\lambda_H}. \quad (100)$$

Note that the relation $dx_H/dt = v_H$ is a consequence of the general statement that the small-amplitude edge of the DSW propagates with the group velocity corresponding to the wave number determined by the solution of the Whitham equations. Indeed, the NLS group velocity of a linear wave with wave vector k moving over a background $\rho_0 = c_0^2$ is the group velocity of the so-called Bogoliubov waves

$$v_g(k) = \frac{k^2/2 + c_0^2}{\sqrt{k^2/4 + c_0^2}}, \quad (101)$$

where $k = 2\pi/L = 2\sqrt{\lambda_H^2 - c_0^2}$ [L is computed from Eq. (56)]. This yields $v_g = 2\lambda_H - c_0^2/\lambda_H = v_H$, as it should. This property of the small-amplitude edge is especially important in the theory of DSWs for nonintegrable equations (see, e.g., Refs. [57,58]).

The value of $W_4^A(\lambda_H, \lambda_H)$ in Eq. (99) is computed through (63) and (90). We get

$$W_4^A(\lambda_H, \lambda_H) = \pi\varphi^A(\lambda_H) + \pi\left(\lambda_H - \frac{c_0^2}{\lambda_H}\right) \frac{d\varphi^A}{d\mu}(\lambda_H) \quad (102)$$

and

$$\begin{aligned} \frac{dW_4^A(\lambda_H, \lambda_H)}{d\lambda_H} &= \pi\left(2 + \frac{c_0^2}{\lambda_H^2}\right) \frac{d\varphi^A}{d\mu}(\lambda_H) \\ &+ \pi\left(\lambda_H - \frac{c_0^2}{\lambda_H}\right) \frac{d^2\varphi^A}{d\mu^2}(\lambda_H), \end{aligned} \quad (103)$$

where φ^A is given by Eq. (89). Once expression (103) has been used to obtain $\lambda_H(t)$ by solving Eq. (100), the position $x_H(t)$ of the harmonic edge of the DSW is determined by (99). The time evolution of $x_H(t)$ is displayed in Fig. 10.

The position of the point $x_m(t)$ where $\lambda_4 = c_m$ (cf. Fig. 9) can be obtained from Eqs. (63). First, for a given time t , we need to find the corresponding value λ_3 , the solution of the equation

$$t = \frac{W_3(\lambda_3, c_m) - W_4(\lambda_3, c_m)}{v_4(\lambda_3, c_m) - v_3(\lambda_3, c_m)}. \quad (104)$$

Note that in this equation we did not write the superscript A or B, because this formula equally holds in both cases since it is to be determined at the boundary between the two regions A and B of the DSW [cf. Eq. (66) and Fig. 9]. Then $x_m(t)$ is determined using either of Eqs. (63). The result is shown in

Fig. 10, where the curve $x_m(t)$ represents the position of the boundary between the two regions A and B at time t .

D. Global picture

We now compare the results of the Whitham approach with the numerical solution of the NLS equation (2) for the initial profile (3). The DSW is described by Whitham method as explained in Secs. IV A and IV B. For this purpose we need to determine λ_3 and λ_4 as functions of x and t (whereas $\lambda_1 = -c_0$ and $\lambda_2 = c_0$). This is performed as follows. First, we pick up a given $\lambda_4 \in [c_0, \lambda_S]$, where λ_S is the value of λ_4 at the soliton edge, the point where the DSW is connected to the rarefaction wave (it has been explained in Secs. V and VIC how to compute it). Second, at fixed t and λ_4 , we find the corresponding value λ_3 as a solution of the difference of Eqs. (63),

$$(v_4 - v_3)t = W_3(\lambda_3, \lambda_4) - W_4(\lambda_3, \lambda_4), \quad (105)$$

where W_3 and W_4 are computed from Eq. (64), with a superscript A or B, as appropriate. Finally, the corresponding value of x is determined by $x = W_3 + v_3 t$ (or equivalently $x = W_4 + v_4 t$). This procedure gives, for each $\lambda_4 \in [c_0, \lambda_S]$ and t , the values of λ_3 and x . In practice, it makes it possible to associate with each (x, t) a couple (λ_3, λ_4) . The results confirm the schematic behavior depicted in Fig. 9.

The knowledge of $\lambda_3(x, t)$ and $\lambda_4(x, t)$ completes our study and enable us to determine, for each time $t > t_{WB}$, $\rho(x, t)$ and $u(x, t)$ as given by the Whitham approach, for all $x \in \mathbb{R}^+$. Denoting by $x^*(t)$ the left boundary of the hump [recall that we concentrate on the right part of the light intensity profile (see Fig. 9)], we have the following.

(i) In the two regions $x \geq x_H(t)$ and $0 \leq x \leq x^*(t)$, we have $u(x, t) = 0$ and $\rho(x, t) = \rho_0$.

(ii) In the dispersionless region $[x^*(t), x_S(t)]$, $u(x, t)$ and $\rho(x, t)$ are computed from (7) in terms of λ^+ and λ^- , which are computed as explained in Sec. III. The profile in this region rapidly evolves to a rarefaction wave [with $\lambda^- = -c_0$ (see Fig. 9)] of triangular shape.

(iii) Inside the DSW, for $x \in [x_S(t), x_H(t)]$, the functions $\rho(x, t)$ and $u(x, t)$ are given by the expression (52), with $\lambda_1 = -c_0 = -\lambda_2$ and λ_3 and λ_4 determined as functions of x and t by the procedure just explained.

The corresponding density profiles are shown in Fig. 12 at different values of time for the initial distribution (3) (with $\rho_0 = 0.5$, $\rho_1 = 1.5$, and $x_0 = 20$). The agreement with the numerical simulation is excellent. The same level of accuracy is reached for the velocity profile $u(x, t)$.

In Fig. 13 we also compare the wavelength of the nonlinear oscillations within the DSW as determined by Whitham approach [Eq. (56)] with the results of numerical simulations. The agreement is again very good.

VII. DISCUSSION AND EXPERIMENTAL CONSIDERATIONS

The different situations we have identified are summarized in Fig. 14, which displays several typical density profiles in a phase space with coordinates ρ_1/ρ_0 and t . The curves $t_{\text{split}}(\rho_1/\rho_0)$ [as given by Eq. (49)] and $t_{WB}(\rho_1/\rho_0)$ [Eq. (72)]

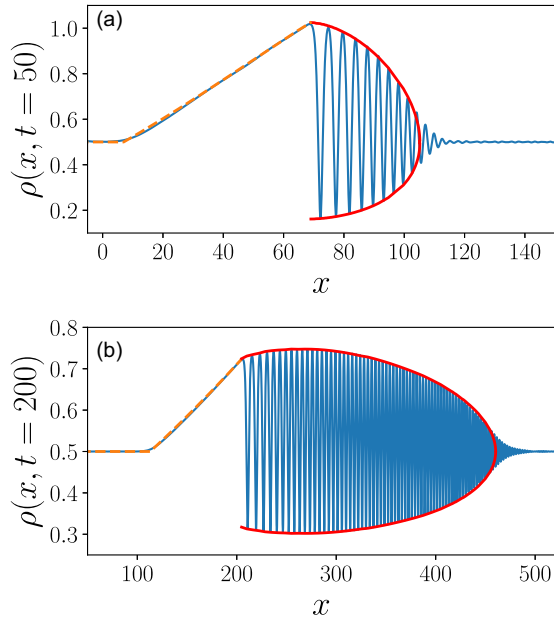


FIG. 12. Comparison between theory and numerical simulations for the density profile $\rho(x, t)$ at (a) $t = 50$ and (b) $t = 200$. The initial profile is the same as that used in all the previous figures. The blue curves are the numerical results. The red solid curves are the envelopes of the density (52) where the λ_i are calculated by the procedure described in Sec. VID. The dashed orange curves correspond to the dispersionless part of the profile, determined using the method given in Sec. III.

separate this plane into four regions, labeled as (a), (b), (c), and (d) in the figure. These two curves cross at a point represented by an open circle whose coordinates we determined numerically as being $\rho_1/\rho_0 = 0.60814$ and $c_0 t/x_0 = 1.09623$. These coordinates are universal in the sense that they have the same value for any initial profile of inverted parabola type, such as given by Eq. (3), with $u(x, 0) = 0$. Other types of initial profile would yield different precise arrangements of these curves in phase space, but we expect the qualitative behavior illustrated by Fig. 14 to be generic, because the different regimes depicted in this figure correspond to physical intuition: A larger initial hump (larger ρ_1/ρ_0) experiences

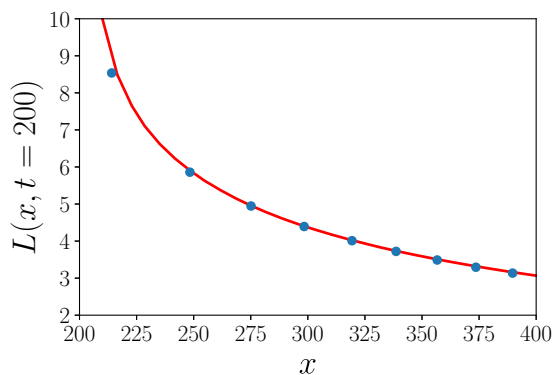


FIG. 13. Wavelength of the nonlinear oscillations within the DSW for $t = 200$. The theoretical red curve is calculated from Eq. (56). The blue points are extracted from simulations.

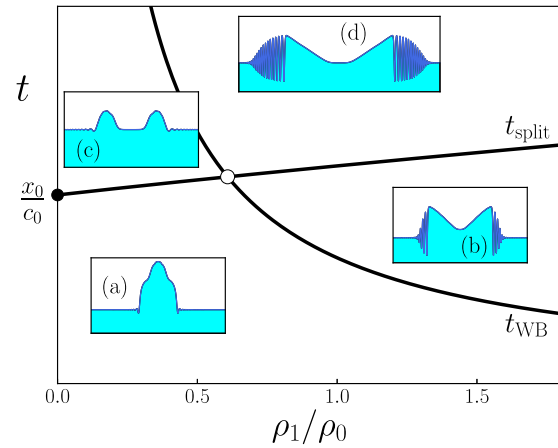


FIG. 14. Behavior of the light intensity profile in the plane $(\rho_1/\rho_0, t)$. The plane is separated into four regions by the curves $t = t_{WB}$ and $t = t_{split}$. These curves cross at the point represented by an open circle (of coordinates $\rho_1/\rho_0 = 0.60814$ and $c_0 t/x_0 = 1.09623$). Typical profiles are displayed in the insets (a)–(d), which represent $\rho(x, t)$ plotted as a function of x for fixed t .

earlier wave breaking and needs a longer time to be separated into two counterpropagating pulses. Also, the evolution of a small initial pulse can initially be described by perturbation theory and first splits into two humps which experience wave breaking in a later stage (as illustrated in Fig. 1): This is the reason why $t_{split} < t_{WB}$ for small ρ_1/ρ_0 . In the opposite situation where $t_{WB} < t < t_{split}$, the wave breaking has already occurred while the profile has not yet split into two separate humps. This is the situation represented by inset (b) and which has been considered in Refs. [15, 18].

In Ref. [18], Xu *et al.* studied the formation of a DSW in a nonlinear optic fiber¹ varying the intensity of the background. In particular, they quantitatively evaluated the visibility of the oscillations near the solitonic edge of the DSW by measuring the contrast

$$C_{ont} = \frac{\rho_{max} - \rho_{min}}{\rho_{max} + \rho_{min}}, \quad (106)$$

where ρ_{max} and ρ_{min} are defined in the inset of Fig. 15. In Ref. [18], the contrast was studied for a fiber of fixed length, for an initial Gaussian bump, i.e., different from (3), keeping the quantities analogous to ρ_1 and x_0 fixed and varying ρ_0 . The experimental results agreed very well with numerical simulations taking into account absorption in the fiber. Here we do not consider exactly the same initial profile and do not take damping into account, but we show that our approach gives a very reasonable analytic account of the behavior of C_{ont} considered as a function of ρ_0/ρ_1 .

From Eq. (52) in the limit $m \rightarrow 1$ (which is the relevant regime near the solitonic edge of the DSW) we get

$$\rho_{max} = \frac{1}{4}(\lambda_S + c_0)^2, \quad \rho_{min} = \frac{1}{4}(\lambda_S - 3c_0)^2, \quad (107)$$

¹In this case the role of variable x in Eq. (2) is played by time, but the phenomenology is very similar to the one we describe in the present work (see, e.g., [59]).

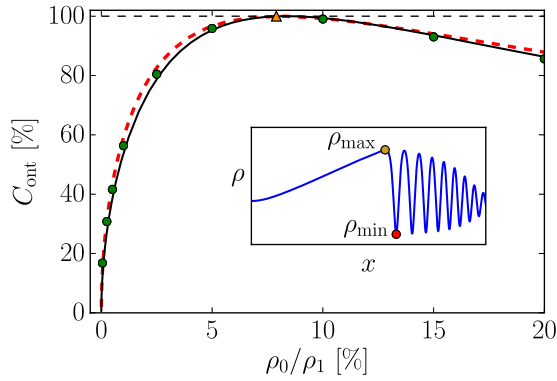


FIG. 15. Contrast C_{ont} represented as a function of ρ_0/ρ_1 . We follow here the procedure of Ref. [18] and use the same dimensionless parameters: The value of ρ_0 varies while $\rho_1 = 5.9$, $x_0 = 6.3$, and $t = 9$ are fixed. The green circles correspond to the numerically determined value of the contrast, obtained from Eq. (106), where ρ_{min} and ρ_{max} are defined as illustrated in the inset. The black solid curve corresponds to expression (108), where λ_S is obtained from (77). The red dashed curve is the approximate result obtained from the same align (108), but evaluating λ_S from Eqs. (81), (110), and (112). The triangle marks the point of contrast unity.

yielding

$$C_{\text{ont}} = \frac{4c_0(\lambda_S - c_0)}{(\lambda_S - c_0)^2 + 4c_0^2}. \quad (108)$$

The results presented in Fig. 15 demonstrate that, as expected, this expression (black solid curve in the figure) agrees very well with the contrast determined from the numerical solution of Eq. (2) (green points).

At this point, the computation of C_{ont} through (108) relies on the determination of λ_S by means of (77), a task which requires a good grasp of the Riemann approach. However, we can get an accurate, though approximate, analytic determination of C_{ont} in a simpler way: by using the large-time expression (81) for λ_S , together with the approximation

$$\begin{aligned} \mathcal{A} &\simeq - \left(\int_{c_m}^{c_0} \sqrt{r - c_0} \frac{dw^B(r)}{dr} dr + \int_{c_0}^{c_m} \sqrt{r - c_0} \frac{dw^A(r)}{dr} dr \right) \\ &= 2 \int_0^{x_0} \sqrt{\lambda^+(x, 0) - c_0} dx. \end{aligned} \quad (109)$$

In the above, we approximated in expression (80) $W_+^{(3/2)}(-c_0, r)$ by $w^{A(B)}(r)$, used the symmetry of these functions, and made the change of variable $x = w^A(r) \Leftrightarrow r = \lambda^+(x, 0)$, in which $\lambda^+(x, 0) = \sqrt{\rho}(x, 0)$, where $\rho(x, 0)$ is the initial density profile (3). A new change of variable yields

$$\mathcal{A} \simeq 2x_0 \sqrt{c_0} F(\rho_0/\rho_1), \quad (110)$$

where

$$F(\alpha) = \int_0^{\pi/2} \cos \theta \left(\sqrt{1 + \frac{\cos^2 \theta}{\alpha}} - 1 \right)^{1/2} d\theta. \quad (111)$$

A simple analytic expression of $F(\alpha)$ cannot be obtained, but we checked that one can devise an accurate approximation by expanding the term in parentheses in the above integrand

around $\theta = 0$ up to second order in θ . This yields

$$\begin{aligned} F(\alpha) &\simeq \frac{(\sqrt{\alpha+1} - \sqrt{\alpha})^{1/2}}{\alpha^{1/4}} \\ &\quad - \frac{\frac{1}{4}(\pi^2/4 - 2)}{\alpha^{1/4} \sqrt{1 + \alpha} (\sqrt{\alpha+1} - \sqrt{\alpha})^{1/2}}. \end{aligned} \quad (112)$$

In the domain $10^{-3} \leq \alpha \leq 50$, $F(\alpha)$ varies over two orders of magnitude (from 4.8 to 7.8×10^{-2}) and the approximation (112) gives an absolute error ranging from 5.8×10^{-2} to 1.8×10^{-3} and a relative one ranging from 1.1% to 2.4%.

Combining Eqs. (108), (81), (110), and (112) yields an analytic expression for the contrast C_{ont} . This expression is represented as a dashed red curve in Fig. 15. As we can see, it compares quite well with the value of C_{ont} extracted from the numerical simulations.² The better agreement with the numerical result is reached for small ρ_0/ρ_1 ; this was expected: In this regime the wave breaking occurs rapidly and we easily fulfill the condition $t \gg t_{\text{WB}}$ where the approximation (81) holds. We note here that the behavior of the contrast illustrated in Fig. 15 is very similar to the one obtained in Ref. [18]. In both cases there is a special value of ρ_0/ρ_1 for which the contrast is unity, meaning that the quantity ρ_{min} cancels. From (107) and (81) this is obtained for $2c_0 \simeq (\mathcal{A}/t)^{2/3}$, i.e., using (110), for

$$\frac{c_0 t}{x_0} = \frac{1}{\sqrt{2}} F(\rho_0/\rho_1). \quad (113)$$

A numerical solution of this equation gives, for the parameters of Fig. 15, a contrast unity when $\rho_0/\rho_1 = 7.9\%$, while the exact Eq. (108) predicts a maximum contrast when $\rho_0/\rho_1 = 8.3\%$ instead (the exact result at $\rho_0/\rho_1 = 7.9\%$ is $C_{\text{ont}} = 0.999$). These two values are marked with a single triangle in Fig. 15 because they cannot be distinguished on the scale of the figure. This shows that the solution of Eq. (113) gives a simple way to determine the best configuration for visualizing the fringes of the DSW; this should be useful for future experimental studies.

Note that formula (108) demonstrates that the contrast depends only on λ_S/c_0 and using the approximate relations (81) and (113) leads to the conclusion that C_{ont} can be considered as a function of the single variable

$$X = \frac{x_0}{t \sqrt{\rho_1}} \sqrt{\frac{\rho_1}{\rho_0}} F(\rho_0/\rho_1). \quad (114)$$

Hence, for a configuration different from the one considered in Fig. 15 but for which the combination of parameters $t \sqrt{\rho_1}/x_0$ takes the same value (namely, 3.47), the curve $C_{\text{ont}}(\rho_0/\rho_1)$ should superimpose on the one displayed in Fig. 15. We checked that this is indeed the case by taking $\rho_1 = 2$, $x_0 = 20$, and $t = 49$, but did not plot the corresponding contrast in Fig. 15 for legibility.

Figure 15 and the discussion of this section illustrate the versatility of our approach which not only gives an excellent

²Computing the contrast using expression (111) instead of the approximation (112) yields a result which is barely distinguishable from the dashed curve in Fig. 15.

account of the numerical simulations at the prize of an elaborate mathematical treatment, but also provides simple limiting expressions, such as Eq. (81), which make it possible to obtain an analytic and quantitative description of experimentally relevant parameters such as the contrast of the fringes of the DSW.

VIII. CONCLUSION

In this work we presented a detailed theoretical treatment of the spreading of a light pulse propagating in a nonlinear medium. A hydrodynamic approach to both the initial nondispersive spreading and the subsequent formation of an optical dispersive shock compares extremely well with the results of numerical simulations. Although in reality the transition between these two regimes is gradual, it is sharp within the Whitham approximation. An exact expression has been obtained for the theoretical wave breaking time which separates these two regimes [Eq. (72)], which may be used to evaluate the experimental parameters necessary to observe a DSW in a realistic setting (see Fig. 14). In addition, our theoretical treatment provides valuable insight into simple features of the shocks which are relevant to future experimental studies, such as the coordinates of its trailing edge x_S , the large-time nondispersive intensity profile which follows it (Sec. V), and the best regime for visualizing the fringes of the DSW (Sec. VII). We note also that our treatment reveals the existence of an asymptotically conserved quantity, see Eq. (84).

A possible extension of the present work would be to consider an initial configuration for which, at variance with the situation we study here, the largest intensity gradient is not reached exactly at the extremity of the initial hump. In this case, wave breaking occurs within a simple wave (not at its boundary) and the DSW has to be described by four position- and time-dependent Riemann invariants [52]. In the vicinity of the wave breaking moment, one of the Riemann invariants can be considered as constant and a generic dispersionless solution can be represented by a cubic parabola; a detailed theory was developed in Ref. [60] for this simpler case. In Refs. [61,62] the general situation was considered for the Korteweg–de Vries equation.

We conclude by stressing that the present treatment focused on quasi-one-dimensional spreading; future developments should consider non-exactly-integrable systems, for instance, light propagation in a photorefractive medium, in a bidimensional situation with cylindrical symmetry.

ACKNOWLEDGMENTS

We thank T. Bienaimé, Q. Fontaine, and Q. Glorieux for fruitful discussions. We also thank an anonymous referee for suggestions that improved the manuscript. A.M.K. thanks Laboratoire de Physique Théorique et Modèles Statistiques (Université Paris–Saclay), where this work started, for kind hospitality. This work was supported by the French ANR under Grant No. ANR-15-CE30-0017 (Haralab project).

-
- [1] V. I. Talanov, *Radiophys.* **9**, 138 (1965).
 - [2] S. A. Akhmanov, A. P. Sukhorukov, and R. V. Khokhlov, *Zh. Eksp. Teor. Fiz.* **50**, 1537 (1966) [*Sov. Phys. JETP* **23**, 1025 (1966)].
 - [3] S. A. Akhmanov, A. P. Sukhorukov, and R. V. Khokhlov, *Usp. Fiz. Nauk* **93**, 19 (1967) [*Sov. Phys. Usp.* **10**, 609 (1968)].
 - [4] S. A. Akhmanov, D. P. Krindach, A. P. Sukhorukov, and R. V. Khokhlov, *Pis'ma Zh. Eksp. Teor. Fiz.* **6**, 509 (1967) [*JETP Lett.* **6**, 38 (1967)].
 - [5] R. G. Harrison, L. Dambly, D. Yu, and W. Lu, *Opt. Commun.* **139**, 69 (1997).
 - [6] P. Emplit, J. P. Hamaide, F. Reynaud, C. Froehly, and A. Barthelemy, *Opt. Commun.* **62**, 374 (1987).
 - [7] D. Krökel, N. J. Halas, G. Giuliani, and D. Grischkowsky, *Phys. Rev. Lett.* **60**, 29 (1988).
 - [8] A. M. Weiner, J. P. Heritage, R. J. Hawkins, R. N. Thurston, E. M. Kirschner, D. E. Leaird, and W. J. Tomlinson, *Phys. Rev. Lett.* **61**, 2445 (1988).
 - [9] F. T. Arecchi, G. Giacomelli, P. L. Ramazza, and S. Residori, *Phys. Rev. Lett.* **67**, 3749 (1991).
 - [10] M. Vaupel, K. Staliunas, and C. O. Weiss, *Phys. Rev. A* **54**, 880 (1996).
 - [11] D. Vocke, K. Wilson, F. Marino, I. Carusotto, E. M. Wright, T. Roger, B. P. Anderson, P. Öhberg, and D. Faccio, *Phys. Rev. A* **94**, 013849 (2016).
 - [12] J. E. Rothenberg and D. Grischkowsky, *Phys. Rev. Lett.* **62**, 531 (1989).
 - [13] N. Ghofraniha, C. Conti, G. Ruocco, and S. Trillo, *Phys. Rev. Lett.* **99**, 043903 (2007).
 - [14] G. Couton, H. Maillotte, and M. Chauvet, *J. Opt. B* **6**, S223 (2004).
 - [15] W. Wan, S. Jia, and J. W. Fleischer, *Nat. Phys.* **3**, 46 (2007).
 - [16] C. Barsi, W. Wan, C. Sun, and J. W. Fleischer, *Opt. Lett.* **32**, 2930 (2007).
 - [17] J. Fatome, C. Finot, G. Millot, A. Armaroli, and S. Trillo, *Phys. Rev. X* **4**, 021022 (2014).
 - [18] G. Xu, A. Mussot, A. Kudlinski, S. Trillo, F. Copie, and M. Conforti, *Opt. Lett.* **41**, 2656 (2016).
 - [19] G. Xu, M. Conforti, A. Kudlinski, A. Mussot, and S. Trillo, *Phys. Rev. Lett.* **118**, 254101 (2017).
 - [20] M. Karpov, T. Congy, Y. Sivan, V. Fleurov, N. Pavloff, and S. Bar-Ad, *Optica* **2**, 1053 (2015).
 - [21] M. Elazar, V. Fleurov, and S. Bar-Ad, *Phys. Rev. A* **86**, 063821 (2012).
 - [22] D. Vocke, C. Maitland, A. Prain, F. Biancalana, F. Marino, E. M. Wright, and D. Faccio, *Optica* **5**, 1099 (2018).
 - [23] J. Drori, Y. Rosenberg, D. Bermudez, Y. Silberberg, and U. Leonhardt, *Phys. Rev. Lett.* **122**, 010404 (2019).
 - [24] D. Vocke, T. Roger, F. Marino, E. M. Wright, I. Carusotto, M. Clerici, and D. Faccio, *Optica* **2**, 484 (2015).
 - [25] Q. Fontaine, T. Bienaimé, S. Pigeon, E. Giacobino, A. Bramati, and Q. Glorieux, *Phys. Rev. Lett.* **121**, 183604 (2018).
 - [26] C. Michel, O. Boughdad, M. Albert, P.-É. Larré, and M. Bellec, *Nat. Commun.* **9**, 2108 (2018).
 - [27] A. M. Kamchatnov, A. Gammal, and R. A. Kraenkel, *Phys. Rev. A* **69**, 063605 (2004).
 - [28] G. A. El, A. Gammal, E. G. Khamis, R. A. Kraenkel, and A. M. Kamchatnov, *Phys. Rev. A* **76**, 053813 (2007).

- [29] M. Conforti and S. Trillo, in *Rogue and Shock Waves in Nonlinear Dispersive Media*, edited by M. Onorato, S. Residori, and F. Baronio, Lecture Notes in Physics Vol. 926 (Springer International, Cham, 2016).
- [30] G. B. Whitham, *Linear and Nonlinear Waves* (Wiley Interscience, New York, 1974).
- [31] M. Isoard, A. M. Kamchatnov, and N. Pavloff, *Phys. Rev. E* **99**, 012210 (2019).
- [32] G. S. S. Ludford, *Proc. Cambridge Philos. Soc.* **48**, 499 (1952).
- [33] M. G. Forest, C.-J. Rosenberg, and O. C. Wright III, *Nonlinearity* **22**, 2287 (2009).
- [34] A. V. Gurevich and L. P. Pitaevskii, *Zh. Eksp. Teor. Fiz.* **65**, 590 (1973) [*Sov. Phys. JETP* **38**, 291 (1974)].
- [35] G. A. El and M. A. Hoefer, *Physica D* **333**, 11 (2016).
- [36] A. V. Gurevich, A. L. Krylov, and N. G. Mazur, *Zh. Eksp. Teor. Fiz.* **95**, 1674 (1989) [*Sov. Phys. JETP* **68**, 966 (1989)].
- [37] A. V. Gurevich, A. L. Krylov, and G. A. El, *Pis'ma Zh. Eksp. Teor. Fiz.* **54**, 104 (1991) [*JETP Lett.* **54**, 102 (1991)].
- [38] A. V. Gurevich, A. L. Krylov, and G. A. El, *Zh. Eksp. Teor. Fiz.* **101**, 1797 (1992) [*Sov. Phys. JETP* **74**, 957 (1992)].
- [39] A. L. Krylov, V. V. Khodorovskii, and G. A. El, *Pis'ma Zh. Eksp. Teor. Fiz.* **56**, 325 (1992) [*JETP Lett.* **56**, 323 (1992)].
- [40] G. A. El and V. V. Khodorovsky, *Phys. Lett. A* **182**, 49 (1993).
- [41] G. A. El, A. M. Kamchatnov, V. V. Khodorovskii, E. S. Annibale, and A. Gammal, *Phys. Rev. E* **80**, 046317 (2009).
- [42] L. D. Landau, E. M. Lifshitz, and L. P. Pitaevskii, *Electrodynamics of Continuous Media*, Landau and Lifshitz Course of Theoretical Physics Vol. 8 (Elsevier Butterworth-Heinemann, Oxford, 2006).
- [43] A. M. Kamchatnov, *Nonlinear Periodic Waves and Their Modulations: An Introductory Course* (World Scientific, Singapore, 2000).
- [44] S. P. Tsarev, *Math. USSR Izv.* **37**, 397 (1991).
- [45] A. Sommerfeld, *Partial Differential Equations in Physics*, Lectures on Theoretical Physics Vol. VI (Academic, New York, 1964).
- [46] *Handbook of Mathematical Functions: With Formulas, Graphs, and Mathematical Tables*, edited by M. Abramowitz and I. A. Stegun (Dover, New York, 1970).
- [47] L. D. Landau and E. M. Lifshitz, *Fluid Mechanics* (Pergamon, Oxford, 1987).
- [48] It should not be a surprise that, to determine the wave breaking time, it is legitimate to replace $W_+^{(3)}(-c_0, \lambda^+)$ by $w^A(\lambda^+)$ in Eq. (45). Indeed, the wave breaking phenomenon occurs when several characteristics issued from the right region of the edge of the bump cross (in region III for the case considered). For all these characteristics, we intuitively expect that we can neglect the weak dependence of λ^- on x . This is indeed the case: We can rigorously show that $W_+^{(3)}(-c_0, \lambda^+)$ and $w^A(\lambda^+)$ coincide in the limit $\lambda^+ = c_0$, which is the relevant one for evaluating (45).
- [49] M. G. Forest and J. E. Lee, in *Oscillation Theory, Computation, and Methods of Compensated Compactness*, edited by C. Dafermos, J. L. Ericksen, D. Kinderlehrer, and M. Slemrod, IMA Volumes on Mathematics and its Applications Vol. 2 (Springer, New York, 1986), p. 35.
- [50] M. V. Pavlov, *Teor. Mat. Fiz.* **71**, 351 (1987) [*Theor. Math. Phys.* **71**, 584 (1987)].
- [51] R. Z. Sagdeev, in *Reviews of Plasma Physics*, edited by M. A. Leontovich (Consultants Bureau, New York, 1966), Vol. 4, p. 23.
- [52] G. A. El and A. L. Krylov, *Phys. Lett.* **203**, 77 (1995).
- [53] O. C. Wright, *Commun. Pure Appl. Math.* **46**, 423 (1993).
- [54] F. R. Tian, *Commun. Pure Appl. Math.* **46**, 1093 (1993).
- [55] L. P. Eisenhart, *Ann. Math.* **120**, 262 (1918).
- [56] G. Arfken and H. J. Weber, *Mathematical Methods for Physicists* (Academic, Orlando, 2005).
- [57] G. A. El, *Chaos* **15**, 037103 (2005); **16**, 029901 (2006).
- [58] A. M. Kamchatnov, *Phys. Rev. E* **99**, 012203 (2019).
- [59] Y. S. Kivshar and G. P. Agrawal, *Optical Solitons* (Academic, San Diego, 2003).
- [60] A. M. Kamchatnov, R. A. Kraenkel, and B. A. Umarov, *Phys. Rev. E* **66**, 036609 (2002).
- [61] G. A. El, A. L. Krylov, and S. Venakides, *Commun. Pure Appl. Math.* **54**, 1243 (2001).
- [62] T. Grava and C. Klein, *Commun. Pure Appl. Math.* **60**, 1623 (2007).